Robust high temperature oxygen sensor electrodes

Lund, Anders

Publication date:
2010

Document Version
Publisher's PDF, also known as Version of record

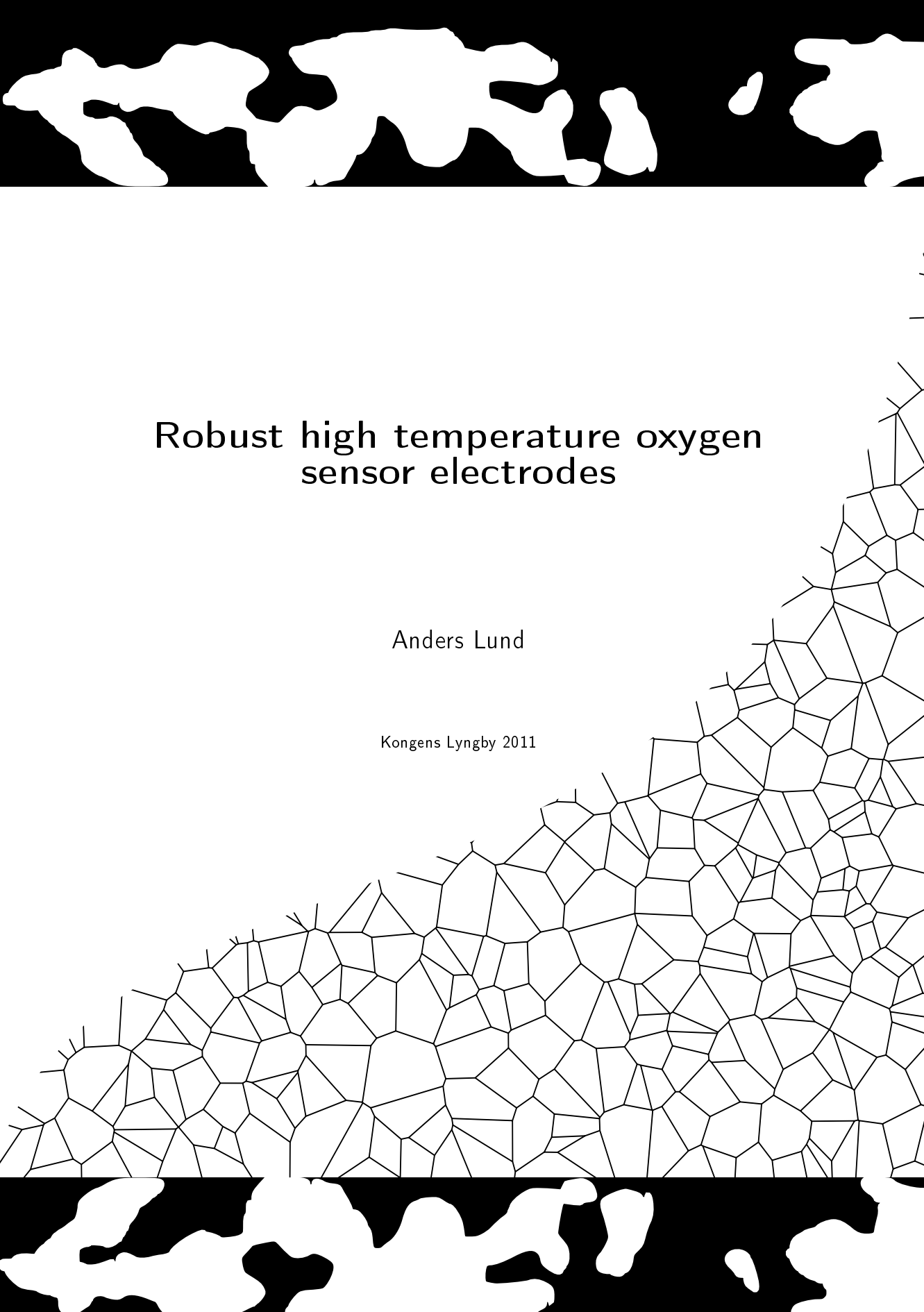

Robust high temperature oxygen sensor electrodes

Anders Lund

Kongens Lyngby 2011

Technical University of Denmark
Department of Chemistry
Kemitorvet, DK-2800 Kongens Lyngby, Denmark
Phone +45 45252419, Fax +45 45883136
isc@kemi.dtu.dk
www.kemi.dtu.dk

Summary

Platinum is the most widely used material in high temperature oxygen sensor electrodes. However, platinum is expensive and the platinum electrode may, under certain conditions, suffer from poisoning, which is detrimental for an oxygen sensor. The objective of this thesis is to evaluate electrode materials as candidates for robust oxygen sensor electrodes. The present work focuses on characterising the electrochemical properties of a few electrode materials to understand which oxygen electrode processes are limiting for the response time of the sensor electrode. Three types of porous platinum-based electrodes and one porous electrode based on the perovskite-structured strontium and vanadium-doped lanthanum chromium oxide (LSCV) were investigated. The porous electrodes were applied on yttrium-stabilised zirconium oxide (YSZ) substrates in a collaboration with the company PBI-Dansensor. The electrochemical properties of the electrodes were characterised by electrochemical impedance spectroscopy (EIS), and the structures were characterised by x-ray diffraction and electron microscopy.

At an oxygen partial pressures of 0.2 bar, the response time of the sensor electrode was determined by oxygen reaction kinetics. At oxygen partial pressures below 10^{-6} bar at 700 °C, the mass transport processes dominated the response time. The response time increased with decreasing oxygen partial pressure and inlet gas flow rate.

A series of porous platinum electrodes were impregnated with the ionically conducting gadolinium-doped cerium oxide (CGO). The addition of CGO was found to decrease the polarisation resistance of the oxygen reaction by up to an order of magnitude compared with a single phase platinum electrode by increasing the effective triple phase boundary (TPB) length. It did not have any significant effect on the response time of the electrode at low oxygen partial pressures. LSCV may take up/release oxygen by changing the oxide ion stoichiometry which gives rise to a large chemical capacitance compared with that of the platinum-based electrodes. The response time of a composite LSCV/YSZ electrode was around an order of magnitude longer compared with that of the platinum-based electrodes electrode. Even though the response time is longer for a composite LSCV/YSZ electrode it may be applied as electrode for oxygen sensors which are used in industrial processes. Furthermore, the platinum-based cermet and the composite LSCV/YSZ electrodes have a longer effective TPB length and are therefore more robust compared with a single phase platinum electrode. The increase in the effective TPB length of the platinum-based electrodes did not have any significant effect on the response time at low oxygen partial pressures, where the response becomes critical.

Resumé

På nuværende tidspunkt er platin det materiale som hyppigst bruges i højtemperatur iltsensor elektroder. Men platin er kostbart og platinelektroden kan under visse betingelser blive forgiftet, hvilket er ødelæggende for iltsensoren. Formålet med denne afhandling er at evaluere elektrode materialer som kandidater til robuste iltsensor elektroder. Der er lagt vægt på at karakterisere de elektrokemiske egenskaber af nogle få elektrodematerialer for at forstå hvordan tilprocesser ved elektroden begrænser responstiden for sensor elektroden. Der blev undersøgt tre forskellige porøse platinbaserede elektroder og en porøs elektrode baseret på strontium og vanadium dopet lanthan krom oxid (LSCV). Elektroderne blev sintret på substrater af yttrium stabiliseret zirconium oxid (YSZ) i samarbejde med virksomheden PBI-Dansensor. De elektrokemisk egenskaber blev undersøgt med elektrokemisk impedans spektroskopi (EIS) og strukturen blev undersøgt med elektron mikroskopi og røntgen diffraktion.
For iltpartialtryk omkring 0.2 bar, var responstiden af elektrode bestemt af ilt reaktionskinetikken. Ved lave iltpartialtryk under omkring 10^{-6} bar ved 700 °C, var responstiden bestemt af masse transportprocesser i gas fasen. Responstiden for iltsensorens elektrode blev længere med faldende iltpartialtryk og indløbs gas flow.
En serie af elektroder blev imprægneret med gadolinium dopet cerium oxid (CGO). Polarisationsmodstanden for iltreaktionen kunne sænkes op til en faktor 10 ved imprægneringen med CGO ved at øge længden af den effektive tre fase grænse (TPB). LSCV kan optage/frigive ilt ved at ændre oxid ion støkiometri, hvilket giver anledning til en høj kapacitans sammenlignet med den der blev målt for de platinbaserede elektroder. Responstiden for en komposit elektrode af LSCV blandet med YSZ var omkring en dekade længere sammenlignet med de platinbaserede elektroder. Selvom responstiden for elektroden med LSCV var væsentligt længere kan den anvendes som elektrode til eksempelvis oxygen sensorer i industrielle processer såsom forarbejdning af fødevarer og i produktion af for eksempelvis silicium-wafers. Endvidere har LSCV/YSZ komposit elektroden samt de platinbaserede elektroder som var imprægneret med CGO eller iblandet YSZ en længere effektiv tre fase grænse og burde derfor være mere robuste sammenlignet med en elektrode der kun indeholder platin. For de platinbaserede elektroder har udvidelsen af den effektive tre fase grænse ikke nogen væsentlig effekt på responstiden ved lave iltpartialtryk, hvor responstiden bliver kritisk.

Preface

This thesis was prepared at the Department of Chemistry at the Technical University of Denmark - DTU and submitted in partial fulfilment of the requirements for obtaining the PhD degree at the Technical University of Denmark. The work lasted from February 2008 to March 2011 and was financed by the Programme Commission on Sustainable Energy and Environment, The Danish Council for Strategic Research, via the Strategic Electrochemistry Research Center (SERC) (www.serc.dk), contract no. 2104-06-0011.

The PhD project was supervised by Prof. M. Mogensen, Dr. T. Jacobsen, Dr. K. V. Hansen and Dr. S. Skaarup, all from DTU, whom I would like to thank for providing me with constant support, encouragement and many useful discussions throughout my time as a PhD student.

I want to thank the Fuel Cells and Solid State Chemistry Division, Risø National Laboratory for Sustainable Energy, DTU in Roskilde for providing the experimental facilities.

Kongens Lyngby 2011

Anders Lund

Papers included in this thesis

I. A. Lund, T. Jacobsen, K. V. Hansen and M. Mogensen, "The effect of loading and particle size on the oxygen reaction in CGO impregnated Pt electrodes", submitted to Journal of Solid State Electrochemistry

II. A. Lund, T. Jacobsen, K. V. Hansen and M. Mogensen, "Limitations of potentiometric oxygen sensors operating at low oxygen levels", submitted to Sensors and Actuators B: Chemical

III. A. Lund, T. Jacobsen, K. V. Hansen and M. Mogensen, "Composite Sr and V-doped $LaCrO_3$/YSZ oxygen sensor electrode", to be submitted

Contents

CHAPTER 1

Introduction

1.1 Solid state oxygen gas sensors

Oxygen sensors are used to monitor the oxygen partial pressure in for example industrial furnaces, boilers, gas turbines and in food packaging.[1–4] The solid state oxygen gas sensor was introduced by Weissbart and Ruka[5] among others in 1960s and is most widely applied in combustion engines to measure the air-to-fuel ratio and thereby increase the efficiency and minimize emission of pollutants. The solid state oxygen gas sensors can be made using various electrochemical principles and they typically operate above 500 °C. The main component is a piece of some oxide ion conducting ceramic material and a set of electrodes which are catalytically active towards oxygen reduction/oxidation.[3,6]

The different types of solid state oxygen sensors most commonly known are; the potentiometric sensor, the diffusion limited amperometric sensor, the resistive sensor and the thermoelectric sensor.[7–10] The potentiometric oxygen sensor cell consist of two porous electrodes separated by a dense electrolyte, Figure 1.1. The cell develops an electromotive force (emf) given by the differ-

ence in oxygen partial pressure at the two electrodes. One of the electrodes is used as a reference and is therefore placed in an atmosphere or in a solid with a known oxygen content.[11] The diffusion limited amperometric sensor uses the principle that a current running through a cell, limited by gas diffusion, is proportional to the oxygen partial pressure.[12] The resistive sensor exploits the oxygen partial pressure dependent conductivity of some metal oxides and the thermoelectric sensor exploits the temperature dependent equilibrium potential.

1.2 The solid state potentiometric oxygen sensor

The solid state potentiometric oxygen sensor is the one most widely used in the industry among others because of its robustness and fast response time. The principles of operation and design have been thoroughly investigated.[13–19] A cross section of the potentiometric oxygen sensor cell is shown in Figure 1.1. Oxygen reacts at the porous electrodes to form oxide ions, which are transported through the electrolyte. The cell develops an emf given by the difference in oxygen partial pressure between the process and reference gas. At equilibrium, there is no current through the cell and the measured voltage difference between the electrodes can be converted to a difference in oxygen partial pressure using the Nernst equation

$$\Delta E_{\mathrm{eq}} = -\frac{\mathrm{R}T}{4\mathrm{F}} \ln\left(\frac{p_{\mathrm{p,O_2}}}{p_{\mathrm{r,O_2}}}\right) \tag{1.1}$$

where $p_{\mathrm{r,O_2}}$ and $p_{\mathrm{p,O_2}}$ refer to the oxygen partial pressure of the reference and the process gas, respectively, R is the gas constant, F is the Faraday constant and T is the temperature of the sensor cell.

The temperature of ideal response depends on the electrochemical properties of the electrodes and the electrolyte and the inlet gas flow rate.[17] A too high flow rate can change the pressure of the gas and have an unwanted cooling effect on the oxygen sensor electrode.[14,20] The difference in the equilibrium potential is proportional to the temperature according to Equation 1.1 where it is assumed that the electrodes are in thermal equilibrium. Errors in the measured temperature lead to errors in the calculated oxygen partial pressure. Furthermore, the temperature should be measured at the measuring electrode and the temperature gradients minimised by choosing a proper furnace.[14] The electrolyte typically consists of yttria stabilised zirconia and the electrodes are

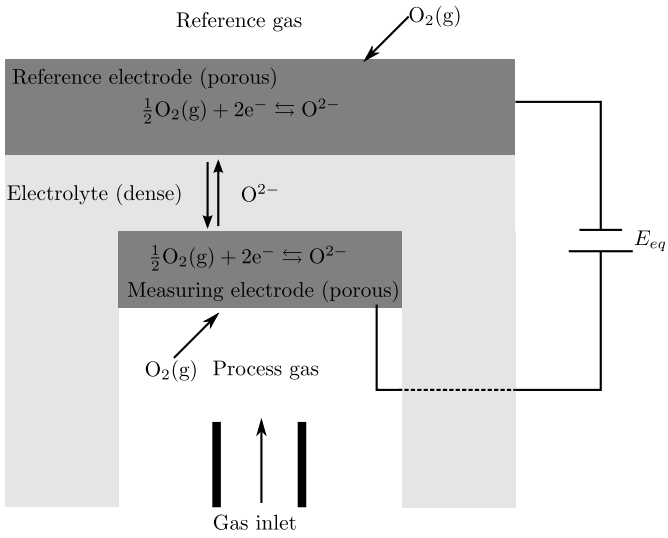

Figure 1.1: Cross-sectional sketch of a potentiometric oxygen sensor cell showing the basic principles. The thickness of the electrode and the electrolyte are not in the right scale.

made from platinum. Using these materials the sensor can in principle be operated in a very large oxygen partial pressure range between around 10^{-30} to 10 bar. However, the measurement becomes problematic at an oxygen partial pressure around 10^{-6} bar in N_2/O_2-mixtures because of a slow response time and because of parasitic reactions that might take place.[19]

1.3 The electrolyte

The electrolyte should be oxide ion conductive and could consist of for example yttria stabilised zirconia (YSZ), gadolinia doped ceria (CGO) or Bi_2O_3. The material most commonly used is yttria (Y_2O_3) stabilised zirconia (ZrO_2), abbreviated YSZ, where 8 mol% zirconia is substituted by yttria. This stabilises the cubic crystal structure and induces formation of oxide ion vacancies.[21] The highest oxide ion conductivity is obtained by substituting with around 8 mol% yttria thereby obtaining an oxide ion conductivity of around 0.16 S cm^{-1} at 1000 °C.[21] The electrolyte must be gas tight to prevent physical permeation of oxygen through the cell. The oxygen sensors may experience rapid cool-

ing which may cause the electrolyte to crack. Partially stabilised zirconia is more mechanically stable and thermal shock resistant compared to YSZ and has therefore also been used as an eletrolyte.[19,22] The YSZ electrolyte also has a small electronic conductivity which leads to a small flow of oxide ions through the cell at equilibrium, which may induce significant errors in the measured potential at oxygen partial pressures around 10^{-6} bar.[17,18] However, the electron hole conductivity is only around 10^{-4} S cm^{-1} at 1000 °C and an oxygen partial pressure of 0.2 bar.

1.4 The electrodes

The electrodes should be catalytically active towards oxygen and electronically conductive. The electrodes should be chemically stable with and have a thermal expansion similar to the electrolyte. Furthermore, changes in the oxide ion stoichiometry, due to changes in the oxygen partial pressure at the measuring electrode, should not affect the volume of that electrode significantly.[23] The electrode should also be corrosion resistant and robust by having a large active area where oxygen can react. Using metal oxide electrodes and a YSZ electrolyte, the potentiometric oxygen sensor may be operated down to around 250 °C.[24]

1.5 Materials

1.5.1 Platinum

Platinum is catalytically active towards oxygen above 500 °C.[25,26] Below this temperature an oxide layer forms on the platinum surface,[27] which inhibits the oxygen reaction kinetics and increases the response time.[19,28] Above 1300 °C, the volatility of platinum will decrease the life time of the electrode.[29] The oxygen reaction of the platinum electrode takes place near the triple phase boundary (TPB) between platinum, electrolyte and gaseous oxygen.[30] The redox reaction of oxygen at the TPB can suffer from poisoning, which means that the reaction is inhibited by adsorption of for example sulphur, silicon dioxide or

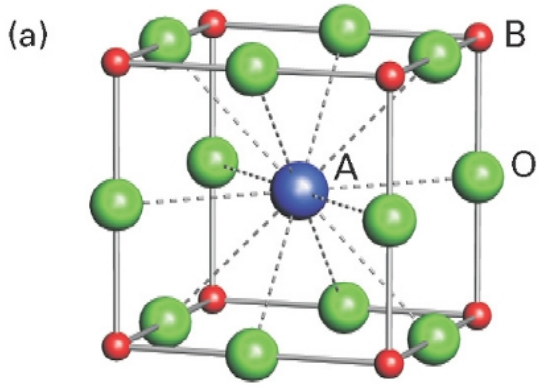

Figure 1.2: Unit cell of the cubic perovskite-type structure (ABO_3) where the blue sphere represents the A-site atom, the red sphere the B-site atom and O the oxide ion. The coordination of the A and B site atoms are shown with lines.

halogens.[25,31,32]

1.5.2 Alternative materials to platinum

A special kind of metal oxides with the general formula ABO_3 are called perovskites after the perovskite mineral $CaTiO_3$. The perovskite structure is illustrated in Figure 1.2 with AO and BO coordination shown with dashed and solid lines, respectively. The perovskite may have a non-cubic structure. The deviation from ideal cubic structure is given by the tolerance factor $t = \sqrt{2}r_{A-O}/2r_{B-O}$ and should lie between 0.75 and 1.0.[23]

By substituting the A-site atom with an atom of lower coordination number, oxide ions vacancies may be created which increases the oxide ion conductivity and the electronic conductivity. The perovskite-type metal oxides can therefore be mixed ionic and electronic conductors (MIECs). The materials are thermally activated semiconductors, however certain materials also exhibit metallic-like conductivity. They have high melting points > 2000 °C and high microstructural and morphological stability compared to platinum and may therefore,

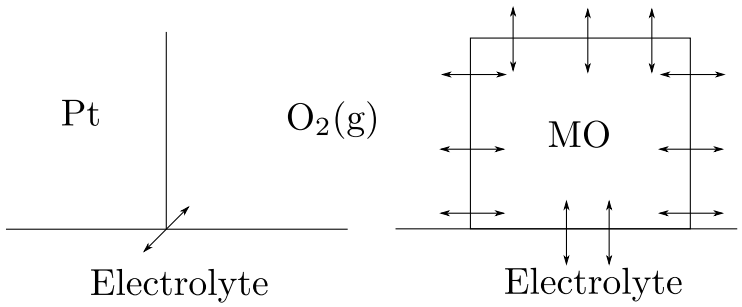

Figure 1.3: The active triple phase boundary of the platinum and the active two phase boundary of the metal oxide (MO).

in principle, be operated at higher temperatures. The materials can take up or release oxygen from the surrounding atmosphere thereby changing the oxide ion stoichiometry, and may be reduced at low oxygen partial pressures.[33] These bulk processes may lead to a slower response time of the electrode due to an increased capacitance. The perovskite-type metal oxides was previously found suitable for different sensor applications.[26,34–42]

Oxygen can react at the surface/gas boundary of the MIEC as shown in Figure 1.3 if the material is catalytically active. The oxygen reaction at the platinum electrode takes place near the triple phase boundary (TPB) between the electrolyte, the platinum and the gas phase.[43–45] Because of the higher active area, the MIECs may be more resistant towards poisoning. Conductivity relaxation experiments have shown that there is a correlation between bulk oxide ion diffusion and the oxygen surface exchange. The catalytic activity towards oxygen increases with the number of vacancies and mobile electronic carries.[30]

The abundance is lower and the demand is higher for platinum compared to the rare earth elements. The raw materials cost of platinum is 64000 US\$ kg^{-1} and that of synthesised perovskite powders are around 500 US\$ kg^{-1}.[46,47] Despite these obvious advantages of metal oxides, the most commonly used electrode material for oxygen sensors in the industry consists of platinum.[3,8,12,48]

1.5.3 Strontium and vanadium-doped lanthanum chromite

Strontium-doped lanthanum chromite (LSC) has previously been suggested as electrode material for potentiometric oxygen sensors.[35,36,42] The A-site doping of $LaCrO_3$ with Sr induces formation of oxide ion vacancies and electron holes thereby increasing the electrical conductivity.[49] The LSC is a p-type thermally activated semiconductor and the electronic transport takes place as a small polaron hopping. The conductivity, σ, depends on the temperature according to $\ln(\sigma T) \propto T^{-1}$.[50] The conductivity is around 30 S cm^{-1} at 700 °C at an oxygen partial pressure of 1 bar.[50] Below $p_{O_2} = 10^{-16}$ bar at 1000 °C, the oxygen vacancy concentration increases exponentially, which leads to a drop in the electron hole conductivity and linear dimensional changes between $0.1 - 0.4\%$ going from an oxygen partial pressure of 0.2 bar at 1000 °C,[51] which could be detrimental for the electrode structure. LSC was found to be catalytically active towards oxygen and was chemically stable in a large oxygen partial pressure-range between 800 and 1000 °C.[42,52]

The LSC has a low oxide ion conductivity, around 10^{-6} S cm^{-1} at 0.2 bar at 1000 °C and because of its high electronic conductivity, it has been considered as a candidate for solid oxide fuel cell interconnects.[53] The LSC should therefore be mixed with an oxide ion conductive material, like for example YSZ, to increase the oxide ion conductivity. The electrode produced should consist of nano-sized LSC grains to increase the active area and decrease the resistance related to transport of oxide ions. The sinterability can be improved by substituting chromium(III) oxide with vanadium(V) oxide (LSCV).[54] By making the material slightly sub stoichiometric on the A-site, the creation of reactive secondary phases can be avoided.[51] Therefore, an electrode with the composition $(La_{0.8}Sr_{0.2})_{0.99}Cr_{0.97}V_{0.03}O_{3-\delta}$ will be used as part of an electrode.

1.5.4 Robust composite electrodes

The length of the triple phase boundary (TPB) can be extended by producing composite electrodes of for example platinum or LSCV mixed with some ionically conductive material, but it may also increase the adhesion of the electrode to the electrolyte. By increasing the TPB and the adhesion, the electrode may become more resistant towards poisoning. Figure 1.4 shows a scanning electron microscope (SEM) micrograph/image of a cross section of a Lambda sensor electrode. The three distinct layers are: a YSZ electrolyte, a porous platinum

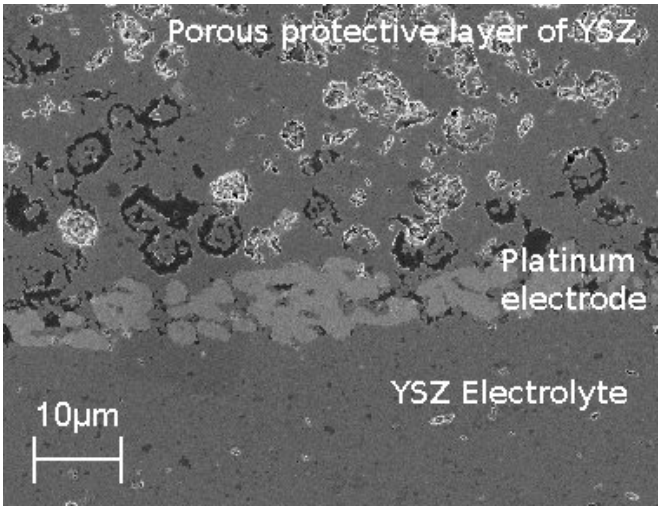

Figure 1.4: SEM micrograph (SE inlens) of a polished cross section of a Lambda sensor electrode, electrolyte and protective layer.

electrode and a porous protective layer of YSZ. The protective layer makes the platinum electrode more resistant towards poisoning because impurities may be adsorbed at the YSZ surface.[55] The composite electrode may have slower time constant, and thereby response time, compared with the single phase electrode.[56]

LSCV can also be mixed with YSZ to increase the sinterability. A composite electrode consisting of LSCV and YSZ will therefore be tested as potential electrode material.

1.6 Collaboration with PBI-Dansensor

The electrodes were produced in a collaboration with the company PBI-Dansensor whom produces potentiometric oxygen sensors for ppm-level detection of oxygen. The company uses the porous platinum electrode and experienced problems due to poisoning of the sensor for some applications and erroneous measurements due to sensor instability. The company is interested in reducing the cost of the sensor while at the same time producing a sensor, which is robust.

By replacing the platinum with an appropriate metal oxide, the material cost may be reduced, in principle. The method of preparation is therefore similar to that used by the company. Their sensors are designed to operate at around 700 °C and at oxygen partial pressures between 10^{-6} and 0.2 bar.

1.7 Objective of the thesis

The Ph.D. work was carried out to study materials for robust oxygen sensor electrodes. There is little known about how oxygen processes at the electrode affect the response time of the electrodes at oxygen partial pressures between 10^{-6} and 0.2 bar. The objective of the thesis was therefore to carry out a detailed characterisation of the electrochemical properties of a few robust electrodes, which are based either on platinum or LSCV.

A series of porous platinum electrodes are impregnated with gadolinia doped ceria (CGO) to improve the electrochemical properties of the platinum electrode, thereby making it more tolerant towards poisoning of the TPB. This is done in a collaboration with the company PBI-Dansensor which produces potentiometric oxygen sensors. The influence of the CGO loading and sintering temperature on the electrochemical properties is characterised by electrochemical impedance spectroscopy (EIS) and the morphology of the electrode is characterised with electron microscopy. In order to study the electrochemical properties at low oxygen partial pressures around 10^{-6} bar an experimental setup was designed and constructed. In this setup composite electrodes of platinum or LSCV mixed with YSZ was tested to study what oxygen processes at the electrode are limiting for the response time of the oxygen sensor at low oxygen partial pressures around 10^{-6} bar. The electrochemical properties of the platinum electrode are also characterised to have a benchmark, to which the electrode with LSCV may be compared.

1.8 Outline of the thesis

The thesis is divided into 7 chapters:

- Chapter 1: Introduction to the potentiometric oxygen sensor and its applications, the materials of interest and the objective of the thesis.
- Chapter 2: Introduction to some of the theoretical concepts used in the thesis.
- Chapter 3: Methods used to prepare and characterise the electrodes.
- Chapter 4: The first paper "The effect of loading and particle size on the oxygen reaction in CGO impregnated Pt electrodes.
- Chapter 5: The second paper "Limitations of potentiometric oxygen sensors operating at low oxygen levels".
- Chapter 6: The third paper: "Composite Sr and V-doped $LaCrO_3$/YSZ oxygen sensor electrode"
- Chapter 7: Summary of the results and concluding remarks.

CHAPTER 2

Theory

The following chapter gives a short introduction to some of the theoretical concepts which are used in the report to analyse the data. The concepts concern the electrochemical properties of the platinum and the LSCV electrode near equilibrium conditions. This is because the potentiometric oxygen sensor operates near equilibrium and only small currents run through the cell at transient conditions. This chapter also has a description of the gas phase mass transport processes at the electrode and how they affect the response time.

2.1 The equilibrium potential

The potentiometric oxygen sensor cell, Figure 1.1, develops an emf given by the difference in oxygen partial pressure between the reference gas and the process gas. The chemical potential of for example gaseous oxygen is defined as

$$\mu_{O_2} = \mu^{\ominus}_{O_2} + RT \ln\left(\frac{p_{O_2}}{p^{\ominus}_{O_2}}\right) \tag{2.1}$$

where $\mu^{\ominus}_{O_2}$ is the standard chemical potential and $p^{\ominus}_{O_2}$ is the standard oxygen partial pressure. At equilibrium, the gradient in the chemical potential of oxygen and the gradient in the electrical potential between the reference and the measuring electrode counteracts each other which cancels the flow of oxide ions through the cell. The difference in the electrical potential between the reference and the measuring electrode is then given by

$$\Delta E_{eq} = E^{r}_{eq} - E^{p}_{eq} = -\frac{RT}{4F} \ln \frac{p_{p,O_2}}{p_{r,O_2}} \tag{2.2}$$

where E^{r}_{eq} and E^{p}_{eq} are the equilibrium potentials and p_{r,O_2} and p_{p,O_2} are the oxygen partial pressures of the reference and the measuring electrode, respectively. This equation is also known as the Nernst equation.

2.2 Reaction kinetics

The description of the oxygen reaction kinetics is limited to that of the platinum electrode since there little known about the oxygen reaction kinetics of the metal oxides. The overall oxygen reaction can be written as

$$O_2(g) + 2V^{\bullet\bullet}_O + 4e^{'} \leftrightarrows 2O^{\times}_O \tag{2.3}$$

using Kröger-Vink notation where $V^{\bullet\bullet}_O$ represents an oxide ion vacancy, e' an electron and $O^{\times}_O$ an oxide ion. The oxygen reaction near the TPB probably involves some adsorption/desorption process, surface diffusion, a charge reaction and incorporation of oxide ions in the YSZ.[44,45] The relation between the Faradaic current and the overpotential may be calculated according to the Butler-Volmer equation as

$$I_F = i_0 B \left(\exp\left[(1-\alpha) \frac{nF}{RT} \eta \right] - \exp\left[-\alpha \frac{nF}{RT} \eta \right] \right) \tag{2.4}$$

where the overpotential, $\eta = E - E_{eq}$, is the difference between the equilibrium potential and the electrode potential, I_F is the Faradaic current, i_0 is the exchange current density, α is a charge transfer coefficient, n is the number of electrons involved in the reaction and $B = l_{TPB} w_{TPB}$ is the active area, where l_{TPB} is the length of the effective TPB and w is a width of the reaction zone near the TPB. The flow of oxide ions through the YSZ electrolyte, J_O, is proportional to the current density, $i_F = I_F/B = 2FJ_O$. For small overpotentials, $F\eta/RT \ll 1$, Equation 2.4 may be written as

$$i_F = i_0 \frac{nF}{RT} \eta \tag{2.5}$$

using that $\exp(0.5\frac{n\mathrm{F}}{\mathrm{R}T}\eta) \approx 1 + 0.5\frac{n\mathrm{F}}{\mathrm{R}T}\eta$. This is equivalent to the potential-current relationship of an ohmic resistor, where the charge transfer resistance is given by $R_{\mathrm{ct}} = \mathrm{R}T/n\mathrm{F}i_0$. In the following only small overpotentials are considered. For a platinum electrode it may be shown that $i_0 \propto p_{\mathrm{O}_2}^{1/4}$ and $R_{\mathrm{ct}} \propto p_{\mathrm{O}_2}^{-1/4}$, at low oxygen partial pressures, if the reaction order with respect to oxygen is $1/2$.[44]

2.3 Impedance of porous MIEC electrodes

The oxygen reaction is influenced by solid state diffusion of oxide ions/oxide ion vacancies and an oxygen reaction at the surface/gas interface. The reaction mechanism at the surface/gas interface probably involves adsorption of gaseous oxygen, dissociation, charge transfer, surface diffusion and incorporation of oxides into the metal oxide.[23] Furthermore, there is an oxide ion/vacancy reaction at the MIEC/YSZ interface. If we assume that the reaction kinetics at the MIEC/YSZ interface are fast and that the transport of oxide ion vacancies in the MIEC is slow compared to the transport of electrons, the change in the concentration of oxide ion vacancies of the porous MIEC electrode is then given by[57]

$$\frac{\partial \Delta c_{\mathrm{v}}}{\partial t} = \frac{(1-\epsilon)D_{\mathrm{Chem}}}{\gamma_{\mathrm{MIEC}}}\frac{\partial^2 \Delta c_{\mathrm{v}}}{\partial y^2} - k\Delta c_{\mathrm{v}} \tag{2.6}$$

where Δc_{v} is a perturbation of the concentration of oxide ion vacancies, k is the chemical surface rate constant, D_{Chem} is the chemical oxide ion vacancy diffusion coefficient along y, γ_{MIEC} is a tortuosity factor and ϵ is the porosity. Both the tortuosity and the porosity depend on the microstructure of the electrode. The chemical diffusion coefficient of oxide ions in LSCV is around 10^{-5} cm^2 s^{-1}, measured by electrical conductivity relaxation.[51] Equation 2.6 may be solved by Laplace transformation of $\frac{\partial \Delta c_{\mathrm{v}}}{\partial t} = s\overline{\Delta c_{\mathrm{v}}}$, where $s = j\omega$, ω is the angular frequency and j is the imaginary unit. The ratio between an oscillating potential, $E = E_0 \exp[i\omega t]$, and an oscillating current is defined as the impedance. For short alternating current (AC) penetration depths compared with the thickness of the MIEC electrode the impedance is then given by[57]

$$Z_{\mathrm{MIEC}} = \frac{\mathrm{R}T\Gamma}{4\mathrm{F}c_{\mathrm{V}}^0}\sqrt{\frac{\gamma_{\mathrm{MIEC}}}{(1-\epsilon)D_{\mathrm{Chem}}k(}\frac{1}{1+(j\omega)/k)}} \tag{2.7}$$

where Γ is a thermodynamic factor, $1/2\partial \ln(p_{\mathrm{O}_2})/\partial \ln(c_{\mathrm{v}})$ and c_{V}^0 is the concentration of oxide ion vacancies at equilibrium. The impedance is equivalent to that

of a Gerischer-type element and may also be observed for porous electrodes with ionic and electronic conducting phases, where the oxygen reaction can take place along the pore.

2.3.1 Capacitance related to stoichiometric changes

The metal oxides take up or release oxygen by changing the oxide ion stoichiometry, $3-\delta$, and may therefore form an oxygen storage. In the following the oxide ion vacancies/oxide ions and the electron/electron holes are considered to be mobile and the cations/cation vacancies to be stationary. The reaction related to the changes in oxide ion stoichiometry may then be written as[51]

$$2\mathrm{Cr}_{\mathrm{Cr}}^{\times} + \frac{1}{2}\mathrm{O}_2 + \mathrm{V}_{\mathrm{O}}^{\bullet\bullet} \leftrightarrows \mathrm{O}_{\mathrm{O}}^{\times} + 2\mathrm{Cr}_{\mathrm{Cr}}^{\bullet} \tag{2.8}$$

The chemical capacitance per unit volume related to a change in the oxide ion stoichiometry is given by

$$C_{\mathrm{Chem}} = -2\mathrm{F}\frac{dc_{\mathrm{V}}}{d\mathrm{E}} \tag{2.9}$$

where c_{V} is the concentration of oxide ion vacancies. Assuming equilibrium is obtained, $E = E_{\mathrm{eq}}$, the differentiated potential may then be written as

$$dE_{\mathrm{eq}} = \frac{\mathrm{R}T}{4\mathrm{F}}\frac{1}{p_{\mathrm{O}_2}}dp_{\mathrm{O}_2} \tag{2.10}$$

The chemical capacitance may be written as

$$C_{\mathrm{Chem}} = -\frac{8\mathrm{F}^2}{\mathrm{R}T}\frac{dc_{\mathrm{V}}}{d\ln(p_{\mathrm{O}_2})} = -\frac{8\mathrm{F}^2}{\mathrm{R}T}c_{\mathrm{V}}^0\frac{d\ln(c_{\mathrm{V}})}{d\ln(p_{\mathrm{O}_2})} \tag{2.11}$$

where c_{V}^0 is the concentration of vacancies at equilibrium. The substitution of $\mathrm{La}_{\mathrm{La}}^{\times}$ with $\mathrm{Sr}_{\mathrm{La}}^{\prime}$ induces formation of oxide ion vacancies and thereby increases the chemical capacitance of LSCV.[58] Figure 2.1 shows the oxide ion stoichiometry, $3-\delta$, as a function of the oxygen partial pressure for some perovskite-type metal oxides of the form $\mathrm{La}_{1-\mathrm{x}}\mathrm{Sr}_{\mathrm{x}}\mathrm{MO}_{3-\delta}$, where M is either Co, Fe, Cr or Mn, at 1000 °C. It is seen that the chromite has the most stable oxide ion stoichiometry between 10^{-6} and 0.2 bar. The LSC also has the smallest amount of oxide ion vacancies and would therefore have the lowest chemical capacitance.[59]

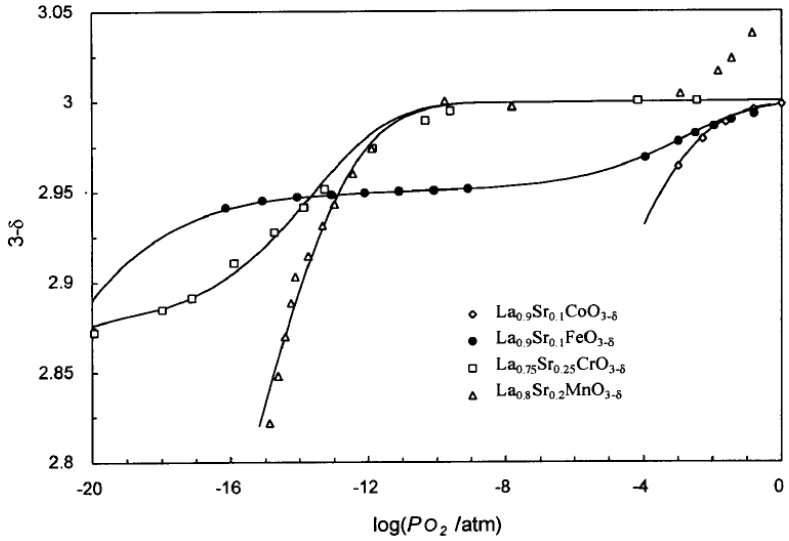

Figure 2.1: Data of the oxide ion non-stoichiometry of $La_{0.75}La_{0.8}Sr_{0.2}MnO_{3-\delta}$, $Sr_{0.25}CrO_{3-\delta}$, $La_{0.9}Sr_{0.1}FeO_{3-\delta}$, $La_{0.9}Sr_{0.1}CoO_{3-\delta}$, at 1000 °C as a function of oxygen partial pressure. (Van Hassel *et al.*[59])

2.4 Gas phase mass transport processes

The gas phase mass transport processes may dominate the electrochemical properties at low oxygen partial pressures and may therefore limit the response time of the oxygen sensor.[60] The gas phase mass transport processes are dependent on the geometry of the sensor setup at the electrode and the inlet gas flow rate. For the closed-end tube sensor shown in Figure 1.1, a stagnant gas layer may be formed above the electrode. The layer may divided into a gas diffusion and a perfectly mixed continuously stirred layer. The impedance of the mass transport processes is then given by[60]

$$Z_{\mathrm{mt}} = \frac{Z_{\mathrm{D}} + Z_{\mathrm{C}}}{1 + \frac{Z_{\mathrm{C}}}{R_{\mathrm{D}}}\sqrt{\tau_{\mathrm{D}} i\omega}\tanh[\sqrt{\tau_{\mathrm{D}} i\omega}]} \tag{2.12}$$

where Z_{D} is the diffusion impedance which is given by

$$Z_{\mathrm{D}} = \frac{R_{\mathrm{D}}}{\sqrt{\tau_{\mathrm{D}} i\omega}}\tanh[\sqrt{\tau_{\mathrm{D}} i\omega}] \tag{2.13}$$

where R_{D} is the gas diffusion resistance, τ_{D} is the characteristic time of the gas diffusion process. The diffusion resistance is inversely proportional to the oxygen partial pressure. Z_{C} is the gas conversion impedance which is equivalent to the impedance of an RC-circuit

$$Z_{\mathrm{C}} = \frac{1}{\frac{1}{R_{\mathrm{C}}} + i\omega C_{\mathrm{C}}} \tag{2.14}$$

where R_{C} is the gas conversion resistance and C_{C} is the gas conversion capacitance. The conversion resistance is inversely proportional and the capacitance proportional to the oxygen partial pressure. The gas conversion time constant is proportional to the volume of the continuously stirred layer, V, and inversely proportional to the inlet gas flow rate, J_{i},

$$\tau_{\mathrm{C}} \propto \frac{V}{J_{\mathrm{i}}} \tag{2.15}$$

To ensure a short response time, the volume of the stagnant gas layer should therefore be small and the inlet gas flow rate high. The characteristic time of the gas diffusion process is given by

$$\tau_{\mathrm{D}} = l_{\mathrm{D}}^2 / D_{\mathrm{eff}} \tag{2.16}$$

where l_{D} is the diffusion boundary length and $D_{\mathrm{eff}} = \epsilon D_{12}/\gamma_{\mathrm{p}}$ is the effective diffusion coefficient, γ_{p} is the tortuosity factor of the pores and D_{12} is the binary gas diffusion coefficient. The mass transport processes are nearly independent of the temperature.

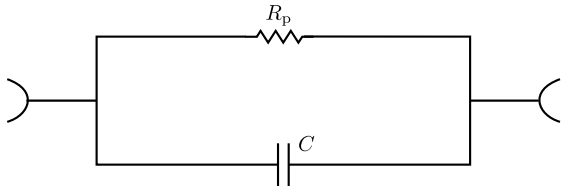

Figure 2.2: An *RC*-circuit representing the oxygen reaction where R_p is a polarisation resistance and C is an apparent capacitance.

2.5 Response time and equivalent circuit modelling

When the electrical potential at the measuring electrode is changed it will take a certain time before equilibrium is obtained because of capacitive contributions. The measured potential then becomes a function of time like for example

$$\Delta E = \sum_i \Delta E_i \exp\left(-t/\tau_i\right) \tag{2.17}$$

where ΔE_i is the potential difference at $t = 0$ of process i, τ_i is the time constant of process i and t is the time. The response time should be as short as possible depending on the application.

The time constant of the various processes may be obtained by EIS in a large range of frequencies.[30] The oxygen processes are modelled using electrical circuits like for example the *RC*-circuit, Figure 2.2, where the polarisation resistance, R_p, represents the ratio between the potential difference across the circuit and the Faradaic current density. In the following, the resistance is normalised with respect to the nominal area of the electrode. The current density, i, can then be expressed as a sum of the Faradaic current density and the current density charging an apparent capacitor, i_C,

$$i = i_F + i_C \tag{2.18}$$

where the capacitance is related to the current density as $i_C = C\frac{d\Delta E}{dt}$.

The impedance of a capacitor is given by

$$Z = \frac{1}{Cj\omega} \tag{2.19}$$

and it is seen that $Z \to 0$ for $\omega \to \infty$ and $Z \to \infty$ for $\omega \to 0$. The imaginary number j denotes that the phase of the response is shifted $1/j\omega \Rightarrow 90\,^0$. The

angular frequency is equal to $2\pi f$, where f is the frequency applied by the current source. The capacitive properties can seldom be described by a simple capacitance and the deviations are accounted for by introducing the constant phase element which has an impedance given by[61]

$$Z_{\mathrm{Q}} = \frac{1}{Q(j\omega)^n} \tag{2.20}$$

where n is a number between 0 and 1. For $n = 1$, Z_{Q} is equal to the impedance of a capacitor and for $n = 0$, Z_{Q} is equal to the impedance of a resistor. The impedance of a resistor does not depend on the frequency. A deviation from a perfect capacitance represents a distribution of relaxation times.[61] The calculated and normalised calculated impedance of an RQ-circuit, $Z_{\mathrm{RQ}} = \frac{1}{\frac{1}{R_{\mathrm{p}}}+Q(j\omega)^n}$, is shown in Figure 2.3 with a characteristic frequency of 10 Hz. The characteristic frequency is given by

$$f = (R_{\mathrm{p}}Q)^{-1/n}/2\pi \tag{2.21}$$

Figure 2.3a shows the Nyquist plot where the imaginary part of the impedance, Z'', is plotted as a function of the real part of the impedance, Z', in a range of frequencies. The Bode plot in Figure 2.3b shows the imaginary part and Figure 2.3c the real part of the impedance as a function of the frequency. The RQ-circuit is shown in Figure 2.3d. It is seen that a decrease in n corresponds to a depression of the semi-circle/arc in the Nyquist plot. The intersection between the impedance and the real-axis of the Nyquist plot at low frequencies gives the DC resistance, in this case R_{p}.

The impedance of a porous mixed ionic and electronic conducting (MIEC) electrode or a porous cermet electrode may be represented by a Gerischer-type element.[57,62] The impedance of the Gerischer-type element is given by $Z_{\mathrm{G}} = R_{\mathrm{G}}\sqrt{\frac{1}{1+\tau^n(j\omega)^n}}$, where the depression of the arc is also accounted for by the exponent n. Figure 2.4a shows the Nyquist plot of the calculated impedance for a model circuit, $(R_{\mathrm{s}})(L)(G)$, consisting of a series combination of an inductance, L, a series resistance, R_{s}, and a Gerischer-type element, G, for different values of the inductance. The series resistance represents the ohmic loss due to transport of oxide ions in the electrolyte and the inductance represents high frequency inductive effects and instrumental artefacts. The bode plot of the imaginary part and the real part of the impedance is shown in Figure 2.4b and Figure 2.4c and the model circuit is shown in Figure 2.4d. Inductive effects can change the point at which the impedance intersects with the x-axis and therefore it may require some modelling to determine the actual series resistance.

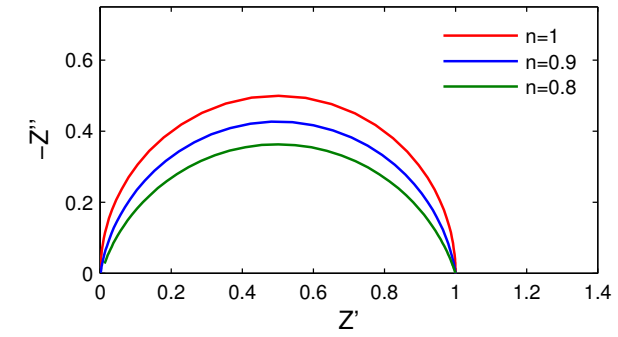

a

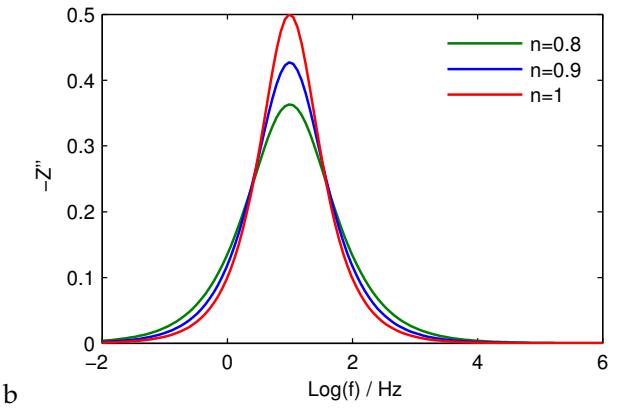

b

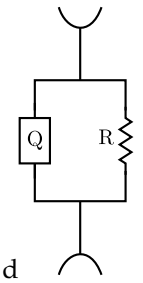

d

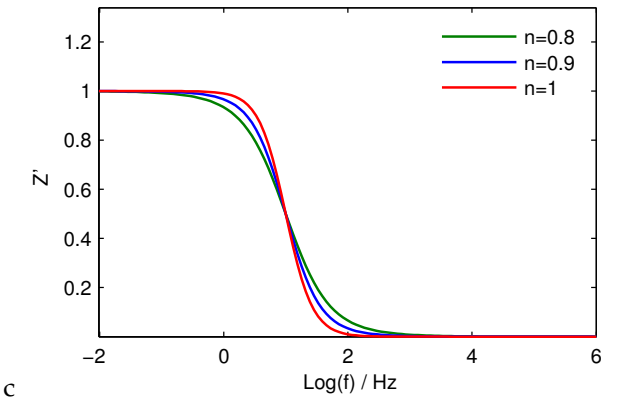

c

Figure 2.3: The calculated impedance of an RQ-circuit for different values of n, a)3 the Nyquist plot, b) the Bode plot of the imaginary part of the impedance and c) the Bode plot of the real part of the impedance and d) the RQ-circuit.

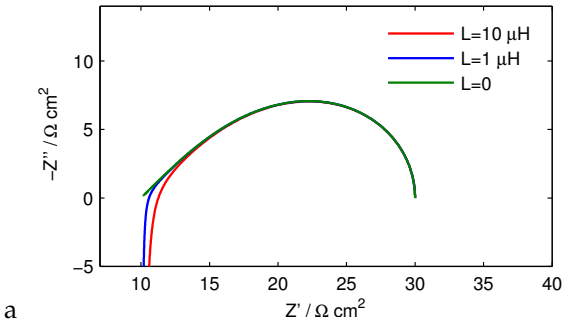

a

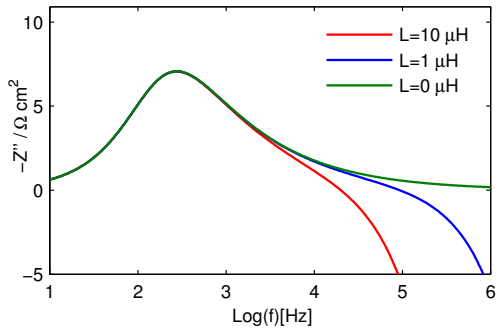

b

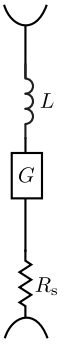

d

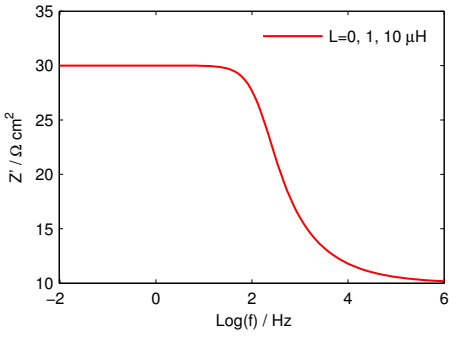

c

Figure 2.4: a) Nyquist plot of the impedance calculated using the model $(R_s)(L)(G)$ for different values of the inductance. $R_G = 20\ \Omega\ cm^2$, $\tau = 10^{-3}$ s, $n = 1$, $R_s = 10\ \Omega\ cm^2$. b) A Bode plot of the imaginary part of the calculated impedance. c) A Bode plot of the real part of the calculated impedance. d) The circuit of the $(R_s)(L)(G)$ model.

2.6 Electrode microstructure

The electrochemical properties of 4 different types of electrodes are presented in the following section. They resemble the microstructures of some of the electrodes produced. Three of the electrodes are based on platinum and one of the electrodes is based on the LSCV. The electrodes have different microstructures and the text below gives a short description of each microstructure and a consideration of the oxygen reaction at the electrodes. Figure 2.5 shows the cross section of a single phase platinum electrode near the electrode/electrolyte interface. The oxygen reaction probably takes place near the TPB which is highlighted with a green colour. Figure 2.6 shows the cross section of an impregnated electrode where a porous CGO layer is formed on the platinum surface. The percolating CGO phase facilitates transport of oxide ions which increases the effective TPB and the electrode may therefore have a higher active area compared with the single phase platinum electrode. Figure 2.7 shows a cross section of a Pt/YSZ cermet electrode. The percolating YSZ phase in the electrode facilitates transport of oxide ions which increases the active area compared with the single phase platinum electrode. Figure 2.8 shows a cross section of an LSCV/YSZ composite electrode. The surface of LSCV exposed to the gaseous phase is active because oxygen may react at the surface/gas interface of the LSCV and the LSCV/YSZ electrode therefore has a higher active area compared with the single phase platinum electrode.

The figures illustrate different ways of how the active area of the electrode may depend on the microstructure. The single platinum electrode has the smallest active area of all the electrodes shown. Impregnation with CGO or mixing with YSZ are two different ways of producing a cermet electrode with a longer effective TPB and thereby a larger active area. The LSCV/YSZ electrode may have an even larger active area because oxygen may react at the LSCV/gas interface.

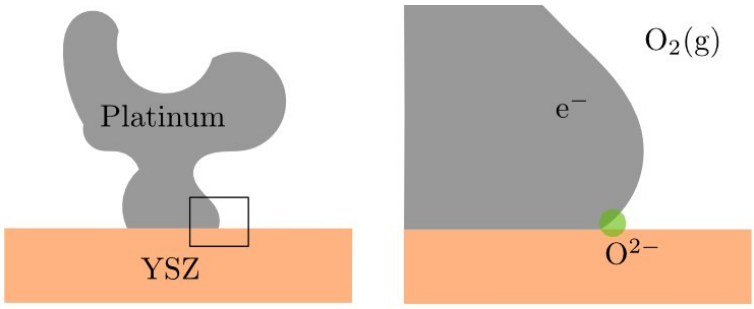

Figure 2.5: A cross section of the single phase electrode. The active area is highlighted with green colour.

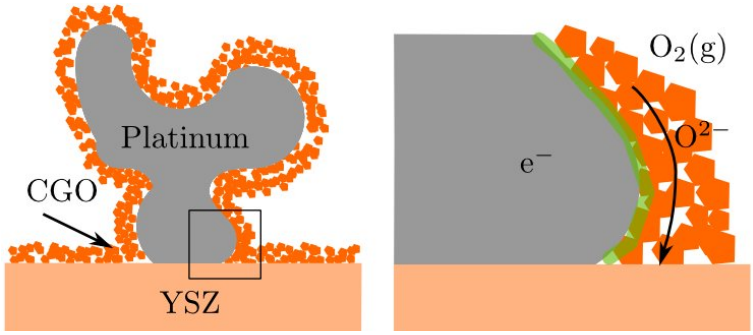

Figure 2.6: A cross section of an impregnated electrode for which a layer of CGO is formed on the platinum surface. CGO grains may facilitate transport of oxide ions to the electrolyte. The active area is highlighted with green colour.

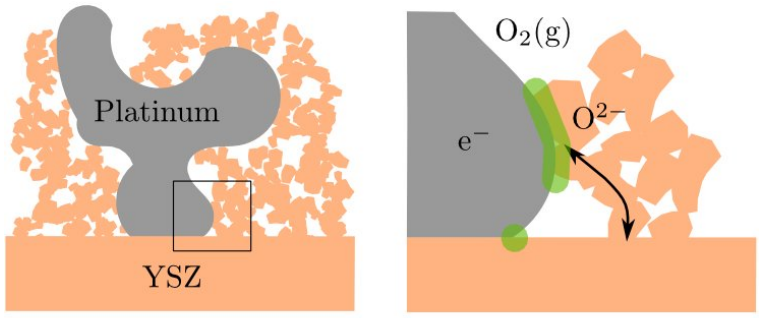

Figure 2.7: A cross section of the Pt/YSZ cermet electrode. Agglomerated YSZ grains facilitates transport of oxide ions. The active areas are highlighted with green colour.

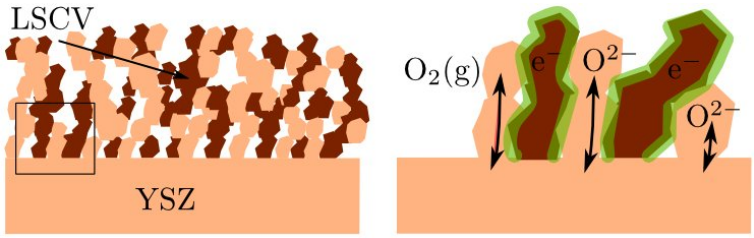

Figure 2.8: A cross section of the LSCV/YSZ composite electrode. YSZ grains facilitate transport of oxide ions. The active area is highlighted with green colour.

CHAPTER 3

Experimental

Four different types of porous electrodes were studied, Table 3.1. The single phase platinum electrodes, (Pt) and the CGO impregnated platinum electrodes (Pt/CGO) were prepared on YSZ tapes to produce symmetrical cells and the composite Pt/YSZ and LSCV/YSZ electrodes were painted on YSZ 3-electrode pellets. The electrochemical properties of the symmetrical cells were characterised in a symmetrical cell setup and the Pt/YSZ and LSCV/YSZ electrodes were characterised using a 3-electrode setup. The 3-electrode setup, was constructed to study the electrochemical properties of the various electrodes in a controlled atmosphere at oxygen partial pressures around 10^{-6} bar. This chapter gives a short description of how the electrodes were prepared and characterised.

Electrodes	Geometry	Test setup
Pt	Tapes	Symmetrical
Pt/CGO	Tapes	Symmetrical
Pt/YSZ	3-electrode pellet	3-electrode
LSCV/YSZ	3-electrode pellet	3-electrode

Table 3.1: Electrodes characterised, the geometry of the YSZ substrate and the experimental setup in which the electrodes were tested.

3.1 LSCV Powder synthesis

0.6 mol $(La_{0.8}Sr_{0.2})_{0.99}Cr_{0.97}V_{0.03}O_{3-\delta}$ (LSCV) powder was synthesized by pyrolysis of an aqueous solution of metal nitrates (>99% purity, Johnson Matthey) with 144 g glycine.[63] This method of synthesis may be used to produce nano-sized LSCV grains. Vanadium was stabilised in an aqueous solution by complexing with citric acid. The correct proportions of the dissolved metal nitrates and glycine were weighed using a Mettler PJ3600 balance with an accuracy of $\pm$10 mg or less than 0.1% of the total weight. The freshly synthesised powder was ball milled for 1 day and then calcined at 800 °C for 2 h. The perovskite phase was verified by x-ray diffraction. The mean particle size of the powder was measured by light scattering using a Beckman Coulter Particle Size Analyser to be 1 μm.

3.2 Preparations of electrodes

In order to produce porous electrodes, a paste, containing the electrode material was painted on a YSZ substrate. The LSCV/YSZ electrode was produced from a paste of LSCV mixed with 8 mol% YSZ (99.85%, Tosoh Corp.) with a volume ratio between LSCV and YSZ of 1:1. The specific surface area of the LSCV was measured by using the Brunauer, Emmett and Teller (BET) method to be 12 $m^2\ g^{-1}$ which is similar to that of the YSZ powder, around 18 $m^2\ g^{-1}$. The paste was brush painted on a 3-electrode pellet of 8 mol% YSZ and the 3-electrode pellet was painted twice and then sintered at 1200 °C in air for 2 h to produce a porous working/measuring electrode. The sintering was performed using the following temperature profile: heated 50 °C h^{-1} up to 500 °C, kept 5 h at 500 °C, heated 120 °C h^{-1} up to 1200 °C, kept 2 h at 1200 °C, cooled 120 °C h^{-1} to 20 °C.

The Pt/YSZ electrode was produced from a paste of platinum (Engelhard, No: 6082A) mixed with 8 mol% YSZ with a volume ratio between platinum and YSZ of 1:1 that was brush painted on a 3-electrode pellet of 8 mol% YSZ . The platinum grains are around 1 μm in size while the YSZ grains are much smaller. The 3-electrode pellet was painted four times and then sintered at 1200 °C in air for 2 h using a sintering profile similar to the one for the LSCV/YSZ electrode.

3.2.1 Impregnation of porous platinum electrodes

Symmetrical cells were produced from 200 μm thick 8 mole % YSZ tape painted with a Bi-containing platinum paste (Engelhard, No: 6082A) on each side. The cells were heated to 900 °C in air to produce sintered porous platinum electrodes. The tapes were painted and sintered four times to produce 10 ± 5 μm thick electrodes. The tapes were then cut to produce 0.5×0.5 cm^2 symmetrical cells. Some of the platinum electrodes were impregnated with a solution of cerium(IV)nitrate (99.5%, Alfa Aesar) and gadolinium(III)nitrate (99.9%, Alfa Aesar) containing deionised water. Pluronic 123 (P123, BASF) was used as a surfactant and either 2.5 or 10 wt% was added to the solution. Solutions corresponding to two different compositions, $Ce_{0.8}Gd_{0.2}O_{2-\delta}$ (CGO20) and $Ce_{0.9}Gd_{0.1}O_{2-\delta}$ (CGO10), were produced. The impregnated electrodes were dried and excess P123 and nitrates were removed by cleaning the cell surfaces with a paper towel. Nano-sized CGO particles were formed by calcining the electrode at 300 °C in flowing air. The CGO loading was calculated as $c_A = m_{CGO}/2A$, where A is the area of the electrode and m_{CGO} is the mass of CGO. The mass of the CGO added, was determined using a Mettler-Toledo XS205 analytical balance with an accuracy of ± 0.01 mg. Prior to measurements the impregnated electrodes were annealed for 12-24 h to obtain a stable grain size.[64]

3.3 3-electrode setup

Figure 3.1a shows a 3-electrode pellet, which was first described by Winkler *et al.*[65], with the working electrode facing upwards. The area of the working electrode is 0.39 cm^2. A reference electrode is placed inside the 3-electrode pellet, through a hole with a diameter of 0.3 cm, to measure the potential drop at

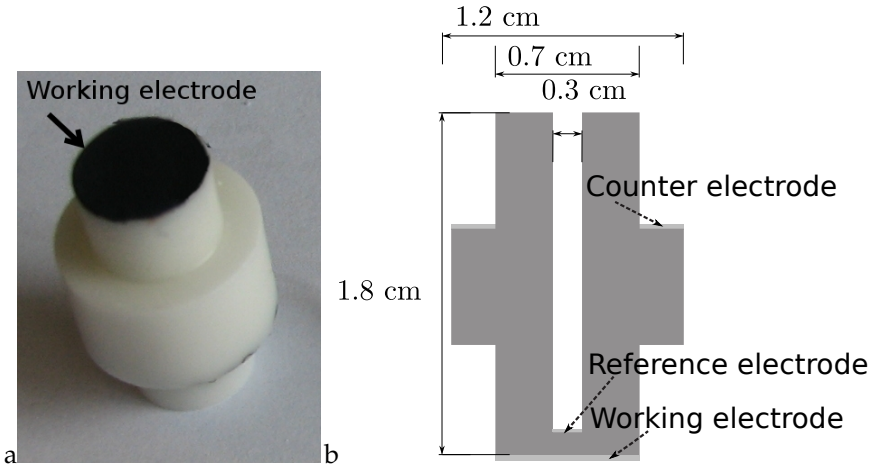

Figure 3.1: a) Image of the 3-electrode pellet with a working electrode pointing upwards. b) Cross section of the 3-electrode pellet and its dimensions.

the working electrode, when a potential has been applied between the working and the counter electrode. Figure 3.1b shows the relative placement of the working, reference and counter electrode and the dimensions of the 3-electrode pellet. The counter and reference electrodes were painted once on the 3-electrode pellet using a platinum paste and were then sintered at 1000 °C for 2 h.

The 3-electrode pellet is placed between two alumina blocks where the lower part is sealed with a gold ring, Figure 3.2a. This part is placed inside a tubular furnace and a Pt-Rh thermocouple is placed near the working electrode to measure and control the temperature. The temperature was measured and controlled using an Eurotherm 2116 temperature controller with an accuracy of ± 1 °C. The setup may be operated up to around 1050 °C and in principle down to room temperature. Both the counter and reference electrode are placed in streaming air, which is used as a reference gas. The process gas is supplied through an inner alumina tube from below.

Figure 3.3 shows the gas flow chart of the rig for the 3-electrode setup. The rig has three Brook Instruments mass flow controllers (MFCs) which are used to control the specific inlet gas flow rate. Two of the MFCs has a range of 1.5 to 15 L h^{-1} and a third has range of 0.06 and 0.6 L h^{-1}. Dry air and dry N_2 were mixed to control the oxygen partial pressure between 10^{-3} bar and 0.2 bar. An oxygen pump was used to control the oxygen partial pressures between 10^{-6}

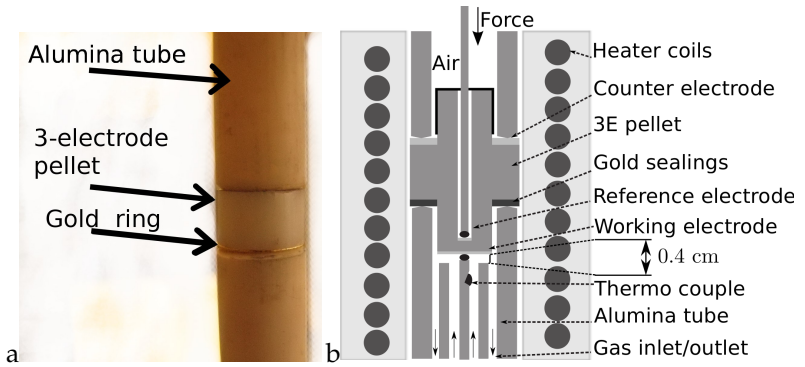

Figure 3.2: a) The 3-electrode pellet between two alumina tubes with the working electrode pointing downwards. A gold ring is used for sealing the lower chamber. This part of the electrode is placed in a furnace. b) Cross section of the 3-electrode setup. The process gas is supplied below through an inner alumina tube and the reference gas is supplied from above. The counter and working electrodes are placed in the reference gas.

and 10^{-3} bar. The oxygen pump consists of a Platinum/YSZ/Platinum cell where oxygen is pumped from air to the N_2 gas by applying an electrical field across the cell using a Potentiostat POT1000M, THJ Instruments. The flow of oxide ions through the cell is then given by $J_O = I/2F$, where I is the electrical current. The oxygen partial pressure can be measured three places; at the oxygen pump/1. oxygen sensor, at the working electrode of the 3-electrode and near the gas outlet using a 2. oxygen sensor. The oxygen partial pressure was obtained by measuring the potential across the oxygen sensor cell using a Keithley 2700 multimeter and the temperature of the measuring electrode, which was held at 700 °C. The potential difference at the 3-electrode was measured between the reference and the working electrode using a Solartron 1255b potentiostat.

3.4 Symmetrical cell setup

Each cell is placed between two alumina blocks with a platinum mesh and pressed together by a load to ensure good electrical contact. Figure 3.4a shows an image of the symmetrical setup, which may be placed inside a tubular furnace, which is closed in one end, with a controlled temperature and atmo-

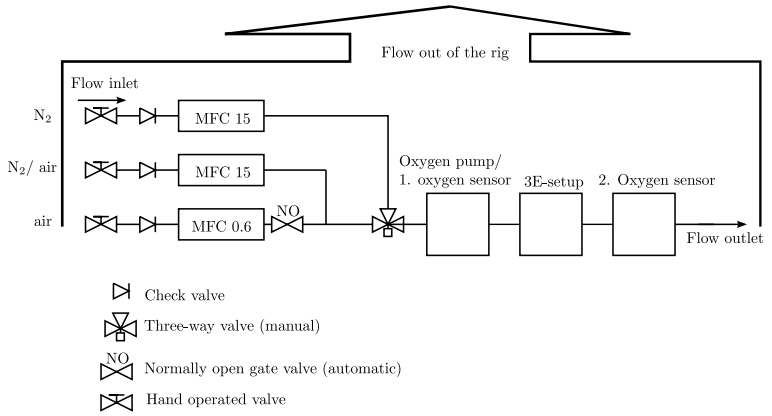

Figure 3.3: Gas flow chart of the 3-electrode test rig. The rig has two mass flow controllers, MFCs, running at a maximum flow rate of 15 L h^{-1} and one with a maximum flow rate of 0.6 L h^{-1}. The gas is sent through an oxygen pump, the 3-electrode setup and then an oxygen sensor before it reaches the outlet.

sphere. A tube, not shown, feeds the inlet gas into the setup next to the alumina blocks. The oxygen partial pressure is measured by an oxygen sensor placed next to the alumina blocks. The temperature is measured at the electrode inside the oxygen sensor tube and near the alumina blocks with an accuracy of ± 1 °C. Figure 3.4b shows the cross section of a symmetrical cell, which has two symmetrical porous electrodes.

3.5 Characterisation methods

3.5.1 Electrochemical impedance spectroscopy

The electrochemical impedance spectroscopy (EIS) measurements on the symmetrical cells were performed using a Solartron 1260 frequency response analyser while a Solartron 1255b frequency response analyser and a Solartron 1287 potentiostat were used to perform measurements on the 3-electrode pellets at open circuit voltage (OCV). The resistance between the counter and the working electrode of the 3-electrode should be small compared to the measuring resistance of the potentiostat. The measurements were performed with an al-

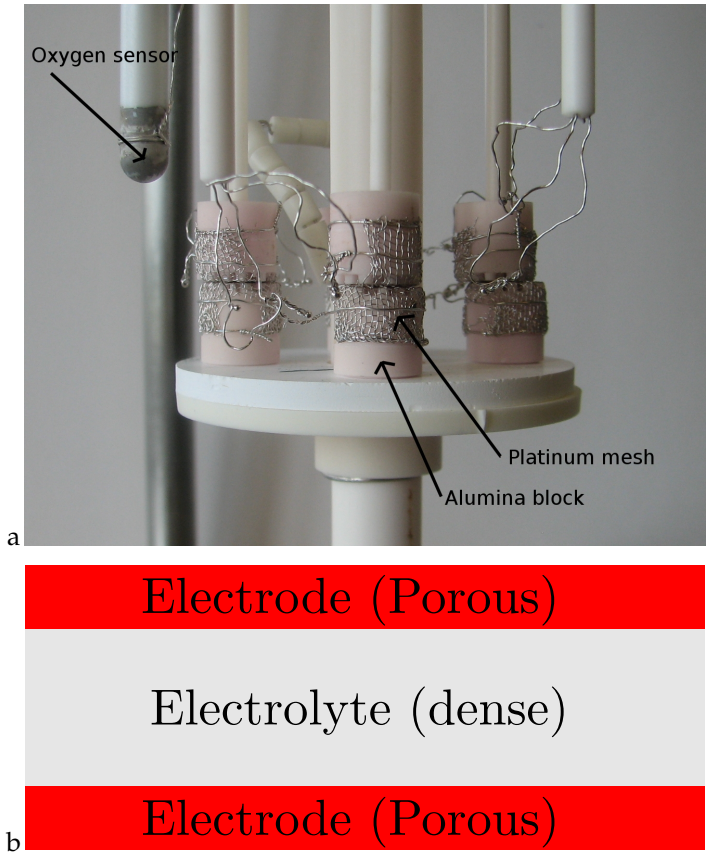

Figure 3.4: a) The symmetrical cell setup which may be placed inside a furnace with a controlled atmosphere where the symmetrical cell is placed between the alumina blocks which are covered with a platinum mesh. b) A cross section of a symmetrical cell, the size of the layers is not in the right scale.

ternating current (AC) root mean square (RMS) amplitude of between 10 and 100 mV, but due to a software error some measurements were performed at 0.5 mV. The amplitude is given by $E_0 = \sqrt{2}E_{\mathrm{RMS}}$, where E_{RMS} is the root mean square amplitude. $E_0\mathrm{F}/\mathrm{R}T \ll 1$ should be fulfilled in order for the linearisation in Equation 2.5 to be valid. The measurements are performed between an AC frequency of around 10^{-3} Hz to 10^5 Hz with between 3 to 20 measurements per frequency decade. The measurements are divided into frequency segments to use specific integration times ranging from around 1000 periods at high frequencies to around 10 periods at low frequencies.

3.5.2 X-ray powder diffraction

The structures of the materials were verified from their characteristic x-ray diffraction patterns. The diffraction patterns were obtained using a Theta-Theta STOE and a Bruker D8 Advance diffractometer using Cu K_α radiation in a 2θ-range between 20° and 90° with a 2θ step size of 0.02° and a counting time between 2 and 5 s per step. The raw peaks were indexed by comparing with experimentally obtained data using the STOE or Bruker software packages. The impurities found were less than 1% and probably related to the formation of secondary phases. The mean grain size, d, can be calculated by applying the Scherrer method to the (111) line, $d = K\lambda/\beta\cos(\theta)$. The shape factor, K, was assumed to be 0.9, θ is the scattering angle, $\lambda = 0.154$ nm is the x-ray wavelength and β is the full width at half maximum of the (111) line. The instrumental broadening was $2\theta \approx 0.05^\circ$.

3.5.3 Scanning electron microscopy

The microstructure and the morphology of the powders and the electrodes were characterised by electron microscopy. The micrographs/images presented here were obtained using the field emission secondary electron microscopes (SEMs), Zeiss SUPRA-35 and Zeiss X-beam 1540 with a secondary electron (SE)-detector. Two different types of SE-detectors were used, an Inlens-detector and an SE2-detector. The inlens detector has a higher spacial resolution compared with the SE2-detector, whereas the SE2-detector gives a better impression of depth in the micrographs. Prior to characterisation, the samples were either fractured or cut with a diamond saw. Some samples were cast into epoxy

and then polished to obtain plane surfaces. The samples may be carbon coated if the material studied is not electronically conductive to prevent charging of the sample.

CHAPTER 4

CGO impregnated Pt electrodes

This chapter was submitted as A. Lund, T. Jacobsen, K. V. Hansen and M. Mogensen, "The effect of loading and particle size on the oxygen reaction in CGO impregnated Pt electrodes ", Journal of Solid State Electrochemistry (2011)

4.1 Abstract

Porous platinum electrodes impregnated with $Gd_xCe_{1-x}O_{2-\delta}$ (CGO) are investigated to characterise how nano sized CGO grains affect the oxygen reaction. Impedance measurements were performed at temperatures between 450 and 750 °C and at oxygen partial pressures of 0.2 and 5×10^{-5} bar for electrodes with various CGO loadings and electrodes annealed at various temperatures. The morphology was characterised by scanning electron microscopy and the CGO grain size was determined from x-ray diffraction peak broadening. The results showed that the polarisation resistance decreased with increasing CGO

loading and increasing annealing temperature. CGO facilitates transport of oxygen ions thereby increasing the effective triple phase boundary. impregnation electrode impedance oxygen platinum

4.2 Introduction

The influence of impurities might be reduced by increasing the TPB length through impregnation of porous platinum with ionically conducting materials like gadolinia doped ceria (CGO). Gadolinium(III) oxide doping of cerium(IV) oxide induces formation of oxygen vacancies and thereby high ionic conductivity.[66,67] The ionic conductivity of nanocrystalline CGO increases with decreasing grain size, going from 36 to 11 nm, but it does not exceed the bulk conductivity of micro-sized crystals.[68] Therefore both the gadolinium(III) oxide doping and the decreasing crystal size may improve the electrochemical properties. Nano sized CGO particles can be produced by impregnation and are used in catalysts because of their ability to release or absorb oxygen quickly.[69,70] However, there are only few investigations of the effect of impregnation with CGO on the oxygen reaction in electrodes.[71–73] The incorporation of ionically conducting metal oxides in Pt cermet electrodes has previously been shown to decrease the activation energy of the charge transfer process and improve the catalytic properties.[15,74,75]

Platinum is the most commonly used material for oxygen sensor electrodes because of its good electrocatalytic properties and stability.[3,8,12,48] The catalytic activity of platinum is reduced heavily below 500 °C and therefore sensors with platinum electrodes are normally operated around 700 °C.[27] Important parameters for the practical application of oxygen sensors are the response time and the sensitivity in particular at low oxygen partial pressures. If the oxygen reaction is too slow it may lead to erroneous measurements. Impurities and the formation of oxide layers on platinum may reduce the active triple phase boundary (TPB) length and slow down the oxygen reaction.

The present paper explores the effect of CGO on the electrochemical properties of porous platinum electrodes on yttria stabilised zirconia (YSZ) electrolytes by impedance spectroscopy. The main focus is to resolve which processes are dominating the electrode impedance for various CGO loadings and CGO grain sizes. The measurements were performed at various temperatures and oxygen partial pressures.

4.3 Experimental

Symmetrical cells were produced from 200 µm thick 8 mole % YSZ tape painted with a Bi-containing platinum paste (Engelhard, No: 6082A) on each side. The cells were heated up to 900 °C in air to produce sintered porous platinum electrodes. The 4×4 cm^2 tapes were painted and sintered four times to produce 10 ± 5 µm thick electrodes on each side of the tape. The tapes were then cut to produce 0.5×0.5 cm^2 symmetrical cells. Some of the platinum electrodes were impregnated with a solution of cerium(IV)nitrate (99.5%, Alfa Aesar) and gadolinium(III)nitrate (99.9%, Alfa Aesar) containing deionized (Milli-Q) water. Pluronic 123 (P123, BASF) was used as a surfactant and either 2.5 or 10 wt% was added to the solution. Solutions corresponding to two different compositions, $Ce_{0.8}Gd_{0.2}O_{2-\delta}$ (CGO20) and $Ce_{0.9}Gd_{0.1}O_{2-\delta}$ (CGO10), were produced. The impregnated electrodes were dried and excess P123 and nitrates were removed by cleaning the cell surfaces using laboratory paper towel. Nano-sized CGO particles were formed by calcining the electrode at 300 °C in flowing air. The CGO loading was calculated as $c_A = {}^{m_{CGO}}/_{2A}$, where A is the area of the cell (with two electrodes) and m_{CGO} is the mass of CGO. Table 4.1 lists the electrodes investigated in this paper. Prior to measurements the impregnated electrodes were annealed for 12-24 h to obtain a stable grain size.[64] The series of electrodes 4.2 to 4.9 were annealed at temperatures between 550 and 750 °C to produce CGO of different grain size. The series of impregnated electrodes 3.5 to 3.9 and 4.19 to 4.23 were annealed at 750 and 706 °C , respectively, to obtain similar grain sizes and different CGO loadings.

The formation of the CGO fluorite structure was verified by X-ray diffraction (XRD) using a Bruker D8 Advance diffractometer and using the Cu K_α radiation. The mean grain size, d, was calculated by applying the Scherrer method to the (111) XRD line of CGO at $2\theta = 29°$.[76] The relation $d = {}^{K\lambda}/_{\beta\cos(\theta)}$ was used. The shape factor, K, was assumed to be 0.9, θ is the scattering angle, $\lambda = 0.154$ nm is the x-ray wavelength and β is the full width at half maximum. The instrumental broadening was $2\theta \approx 0.05°$.

For each electrochemical test up to 4 symmetrical cells were placed in a furnace with an inlet gas flow of 6.0 L/h. The temperature of the furnace was controlled with an accuracy of ± 1 °C The oxygen partial pressure was determined by a potentiometric oxygen sensor positioned next to the symmetrical cells. Each cell was placed between two alumina blocks with a platinum mesh and pressed together by a load to ensure good electrical contact. The impedance of the series of electrodes 4.19 to 4.23 was measured in flowing air at 706 °C.

Table 4.1: List of electrodes investigated. c_A is the loading, N_I is the number of impregnations, c_M is the molar concentration of the cations, T_A is the annealing temperature, w_{P123} is the wt% of P123 in solution, β is the full width at half maximum of the (111) XRD line and d is the grain size obtained from the (111) XRD peak broadening.

Cells	c_A / mg cm^{-2}	N_I	c_M / mole L^{-1}	w_{P123} / wt%	T_A / °C	β / °	d / nm
Pt	-	-	-	-	-	-	-
3.5 (CGO20)	0.46	2	3	10	750	-	-
3.7 (CGO20)	0.54	2	3	10	750	-	-
3.9 (CGO20)	0.63	3	3	10	750	-	-
4.2 (CGO20)	0.51	2	3	10	750	0.42	20
4.5 (CGO20)	0.34	2	3	10	700	0.42	20
4.6 (CGO20)	0.74	2	3	10	650	0.53	15
4.7 (CGO20)	0.65	2	3	10	600	0.55	15
4.9 (CGO20)	0.43	2	3	10	550	0.85	10
4.19 (CGO10)	0.47	2	3.5	2.5	706	-	-
4.20 (CGO10)	0.37	1	2.5	2.5	706	-	-
4.22 (CGO10)	0.17	1	1	2.5	706	-	-
4.23 (CGO10)	0.07	1	0.21	2.5	706	-	-

The impedance of the series of electrodes 3.5 to 3.9 was measured between 500 and 750 °C in flowing air. The impedance of the electrodes 4.2 to 4.9 was measured between 443 °C and the annealing temperature, T_A, in flowing N_2 with oxygen partial pressures of around $5 \cdot 10^{-5}$ bar. The measurement at the highest temperature was performed first and the measurement at the lowest temperature, last. The measurements were performed at open circuit voltage (OCV) with an AC root mean square amplitude of 50-100 mV. A Solartron 1260 frequency response analyser was used to conduct the EIS measurements. The cell impedance was analysed with equivalent circuit modelling by nonlinear least square fitting in MatLab applying the Levenberg–Marquardt algorithm and standard errors were calculated using a confidence interval of 95 %.

Symmetrical cells were fractured to investigate the morphology of a cross section. The SEM investigations were performed using field emission SEM (Zeiss SUPRA-35 & Zeiss X-beam 1540) with a secondary electron (SE) detector.

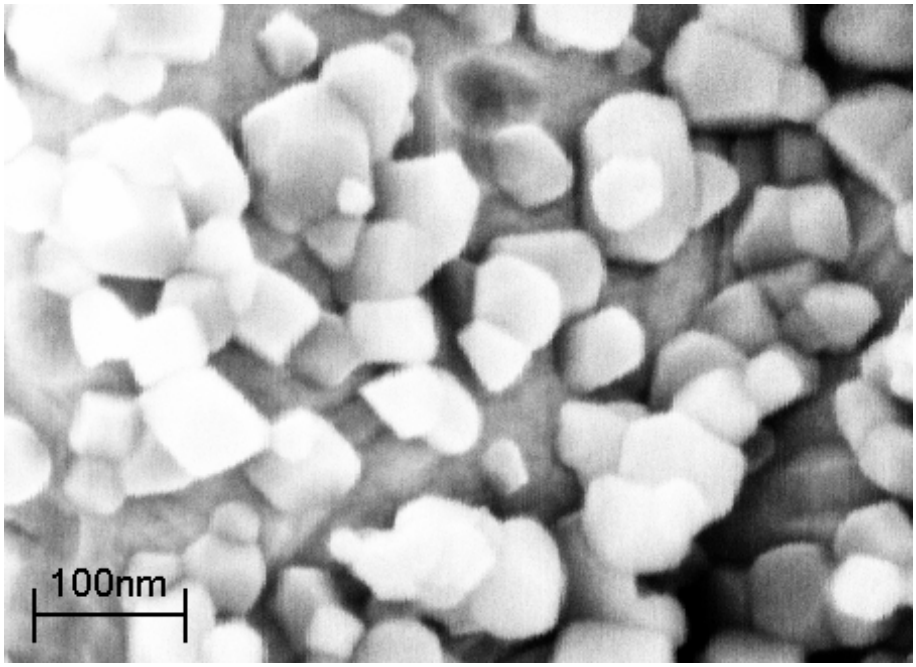

Figure 4.1: SEM (SE) image showing CGO10 grains and agglomerates scattered discretely over a platinum grain, $c_A = 0.37$ mg cm^{-2} and $T_A = 706$ °C (electrode 4.20).

4.4 Results

SEM examination of the impregnated electrode 4.20 showed that most of the CGO10 was found in the pores of the platinum electrode as porous agglomerates and as discrete grains and agglomerates scattered across the surface. Figure 4.1 shows CGO10 grains on the surface of a platinum grain. The electrode, 4.2, in Figure 4.2 was impregnated twice using a higher cation and surfactant concentration compared with the impregnated electrode in Figure 4.1. CGO20 agglomerates were found both in the pores and as a layer, which was around 200 nm thick, on the platinum surface (Figure 4.2). In both electrodes the CGO was distributed uniformly throughout the electrode.

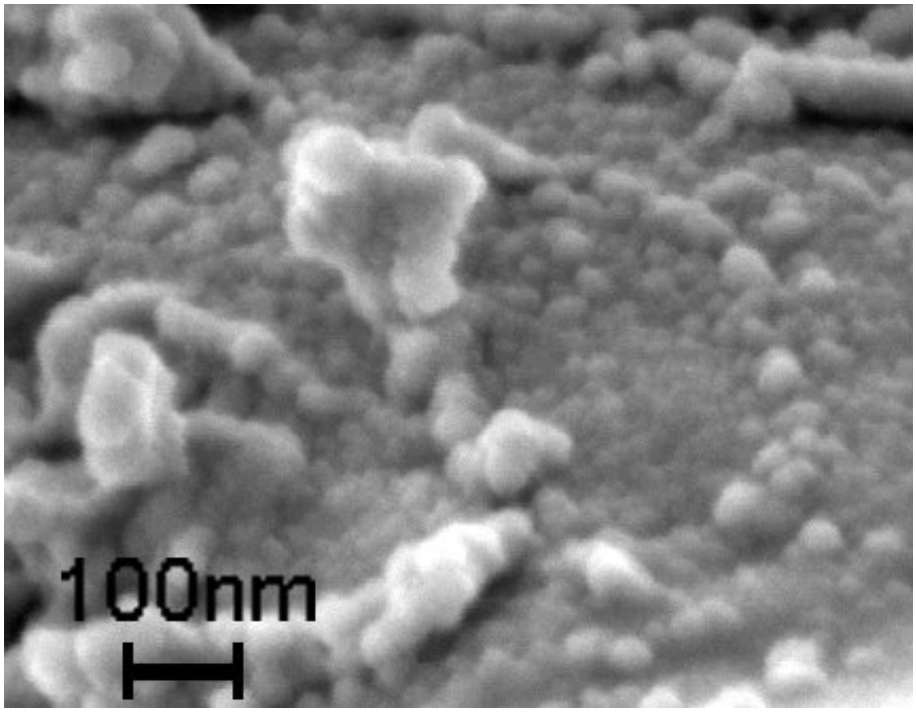

Figure 4.2: SEM (SE) image showing agglomerated CGO20 grains on a platinum grain, $c_A = 0.51$ mg cm^{-2} and $T_A = 750$ °C (electrode 4.2).

4.4.1 EIS measurements in air

Impedance measurements were performed on both CGO10 and CGO20 impregnated electrodes. Figure 4.3 shows the Nyquist plots for CGO10 loadings up to 0.47 mg cm^{-2}. The measurements were performed in a frequency range from 13 Hz and 32 kHz with between 5 and 15 points per decade. The morphology of the electrodes with high loadings, 0.37 mg cm^{-2} and above, was similar to that in Figure 4.2. However, for a loading of only 0.07 mg cm^{-2} the CGO10 was only found as discrete agglomerates. The polarisation resistance decreased with increasing loading of CGO10 until 0.37 mg cm^{-2}. For a higher loading of 0.47 mg cm^{-2}, it was increased. One arc was identified by equivalent circuit modelling for the impregnated and the single phase platinum electrode. The data were therefore fitted with the model $(R_s)(L)(R_eQ_e)$ (Figure 4.3). The equivalent circuit corresponding to the model is shown in Figure 4.3. The series resistance, R_s, represents the ohmic loss due to transport of oxide ions in the YSZ electrolyte and it is frequency independent. The inductance, L, is included to take into account high frequency inductance and instrumental artefacts. The oxygen reaction is represented with an RQ-circuit where R_e is the polarisation resistance and Q_e is the constant phase element. The characteristic frequency of the oxygen reaction was calculated as $2\pi f_e = (R_eQ_e)^{-1/n_e}$ and the apparent capacitance as[77] $C_e = (Q_eR_e^{1-n_e})^{1/n_e}$. The admittance of (R_eQ_e) is given by $Y = 1/R_e + Q_e(i\omega)^{n_e}$. If $n_e = 1$, Q_e has the units of a capacitance and $0 < n_e < 1$ corresponds to a depression of the semicircle in the Nyquist plot.

Table 4.2 lists the results from fitting of R_e, n_e, the characteristic frequency, f_e, and the apparent capacitance, C_e. The addition of CGO10 decreased the polarisation resistance from 3.9 Ω cm^2 for the single phase platinum electrode to 0.7 Ω cm^2 for the electrode with a loading of 0.37 mg cm^{-2}. The polarisation resistance of two identically prepared platinum electrodes was found to be 3.9 and 4.2 Ω cm^2 confirming that the effect of CGO10 is beyond the experimental error. The addition of CGO10 resulted in an increase in the characteristic frequency from 0.46 kHz for the single phase platinum electrode to 2.7 kHz for the electrode containing 0.37 mg cm^{-2}. It had only a small effect on the series resistance R_s and the capacitance, C_e, as given by the table values. The exponent n_e was found to be around 0.9 for the impregnated and the single phase platinum electrode. The capacitance of 88 μFcm^{-2} for the single phase platinum electrode was slightly higher than $20 - 70$ μF cm^{-2} which has previously been reported for the oxygen reaction at the platinum/YSZ interface.[44,78]

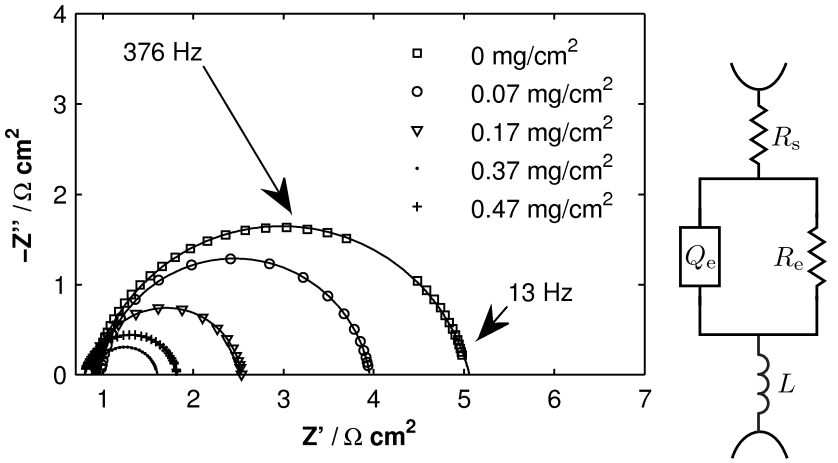

Figure 4.3: Nyquist plot with fits for various loadings of CGO10. The measurements were performed at $p_{O_2} = 0.2$ bar at 706 °C on a single phase platinum electrode and the impregnated electrodes 4.19 to 4.23.

Table 4.2: Fitted parameter values obtained from measurements at 706 °C at an oxygen partial pressure of 0.2 bar on a single phase platinum electrode and CGO10 impregnated electrodes, 4.19 to 4.23.

c_A / mg cm^{-2}	0	0.07	0.17	0.37	0.47
R_s / Ω cm^2	1.0	0.96	0.87	0.89	0.79
R_e / Ω cm^2	3.9	3.0	1.7	0.7	1.0
C_e / μF cm^{-2}	88	69	62	82	78
f_e / kHz	0.46	0.79	1.6	2.7	2.0

CGO20 impregnated electrodes

Figure 4.4 shows the normalised Nyquist plot for measurements performed between 500 and 750 °C at an oxygen partial pressure of 0.2 bar on a CGO20 impregnated electrode, 3.5. The morphology of the electrode was similar to that shown in Figure 4.2. The impedance was measured in a frequency range between 0.5 Hz and 120 kHz with 5 to 10 points per decade. The measurements were fitted with the model $(R_s)(L)(G_e)$, where G_e is a Gerischer-type element. A Gerischer-type impedance can be observed for porous electrodes where reactions are occurring along the interface between an electronic conductor and a ion conductive pore.[79] CGO20 is oxide ion conductive and the CGO20 grains form layers on the platinum as shown in Figure 4.2. The oxygen reaction at the CGO20/platinum interface is represented with an RQ-circuit, (R_eQ_e) and the ohmic loss due transport of oxide ions in the CGO20 phase is represented by a resistor, R_{CGO}. The impedance for an AC signal penetration length which is much smaller than the pore length is then given by

$$Z_G = \left(\frac{R_{CGO}}{\frac{1}{R_e} + Q_e(i\omega)^{n_e}} \right)^{1/2} \tag{4.1}$$

where the total reaction resistance is given by $(R_{CGO}R_e)^{1/2}$. The exponent n_e was between 0.9 and 1. The constant phase element, Q_e, was fixed when fitting using the obtained value of $C_e \approx 80$ μF cm^{-2} from Table 4.2, to decrease the number of free parameters. Figure 4.4 shows that the model fits to the impedance. For the electrode 3.5 (0.46 mg cm^{-2}), R_e was found to be 2.5 Ω cm^2 and R_{CGO} was found to be 0.15 Ω cm^2 at 700 °C .

The addition of CGO20 resulted in a decrease in the total polarisation resistance, $R_p = \sqrt{R_{CGO}R_e}$ from $3.9 - 4.2$ Ω cm^2 for the single phase platinum electrode to $0.60 - 0.74$ Ω cm^2, as given in Table 4.3. Furthermore, it increased the characteristic frequency slightly from $0.37 - 0.48$ kHz for the single phase platinum electrode to $0.39 - 0.6$ kHz. Figure 4.5 shows that the polarisation resistance, R_e, decreases with increasing CGO load up to a loading around 0.4 mg cm^{-2}. The increase in the characteristic frequency, f_e, up to around 0.4 mg cm^{-2} reflects the decrease in the polarisation resistance since the capacitance is not changed significantly. The decrease in the characteristic frequency observed at high loadings may on the other hand reflect a change in the reaction mechanism. The impedance of the impregnated electrodes 3.5 to 3.9 was fitted with a Gerischer type element.

The activation energy of the series resistance, R_s, was found to be $0.7 - 0.9$ eV

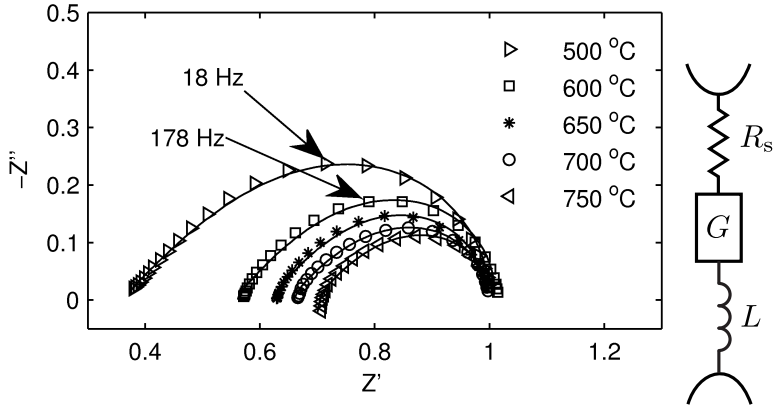

Figure 4.4: Normalised Nyquist plot with fits. The measurements were performed at an oxygen partial pressure of 0.2 bar at various temperatures on the CGO20 impregnated electrode 3.5 (0.46 mg cm^{-2}).

Table 4.3: Fitted parameters obtained from measurements performed at 700°C and an oxygen partial pressure of 0.2 bar on CGO20 impregnated electrodes (3.5-3.9).

c_A/ mg cm^{-2}	0.46	0.54	0.63
R_s/ Ω cm^2	1.1	0.96	0.92
R_p/ Ω cm^2	0.60	0.74	0.66
f_e/ kHz	0.69	0.46	0.39

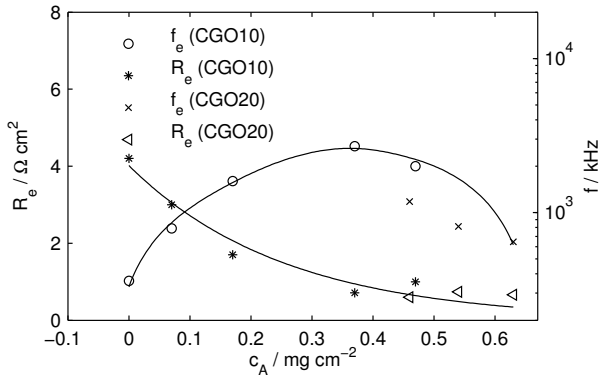

Figure 4.5: The characteristic frequency and polarisation resistance as functions of the CGO loading. The measurements were performed at 700 °C (CGO20) and 706 °C (CGO10) at an oxygen partial pressure of 0.2 bar. The polarisation resistance was fitted with an exponential decaying function.

which is in accordance with the oxide ion resistivity of bulk YSZ.[80] The apparent activation energies of R_e was found to be $1.2 - 1.5$ eV for the impregnated electrodes and it was 2.2 ± 0.3 eV for the single phase platinum electrode. The activation energy obtained for the single phase platinum electrode is in agreement with previous results obtained from impedance spectroscopy by[75]. The activation energy of R_{CGO} was found to be 1.2 ± 0.1 eV for the impregnated electrodes.

4.4.2 EIS measurements in N_2

The series of impregnated electrodes, 4.2 to 4.9 was annealed from 550 to 750 °C to investigate the electrochemical properties as function of the CGO grain size and the annealing temperature. These electrodes were only impregnated with CGO20. The CGO loading was between 0.34 and 0.74 mg cm^{-2} and should therefore have little effect on the polarisation resistance as described earlier. The morphology of the impregnated electrodes was similar to that observed in Figure 4.2. CGO was identified in the XRD from its characteristic diffraction lines. Figure 4.6 shows an almost linear relationship between the mean grain size, d, obtained from XRD peak broadening, and the equilibration temperature. The grain size is in agreement with previous results reported by Levy *et al.*[81] Impedance spectroscopy measurements were performed at an oxygen

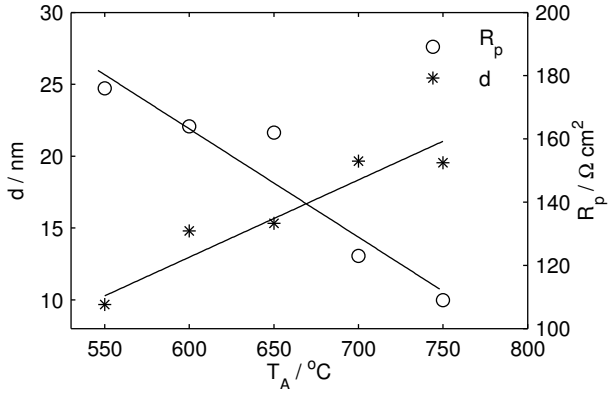

Figure 4.6: The mean grain size, d, measured by XRD peak broadening and the electrode polarisation resistance of the impregnated electrodes 4.2 to 4.9 as functions of the annealing temperature for measurements performed at around 500 °C and at an oxygen partial pressure around 5×10^{-5} bar.

partial pressure of around 5×10^{-5} bar between 443 and 744 °C . Figure 4.6 shows that the polarisation resistance obtained at around 500 °C , decreased with increasing annealing temperature.

Figure 4.7 shows the Nyquist plot obtained at various temperatures from measurements on the impregnated electrode annealed at 700 °C . The measurements were performed in a frequency range from 90 mHz to 10 kHz. At 494 °C and below, a temperature dependent arc dominates the impedance spectrum. This arc is thought to be related to the oxygen reaction and is represented with a Gerischer type impedance as mentioned above. Between 594 and 645 °C a nearly temperature independent arc dominated the impedance spectrum.

The gas phase mass transport processes, gas diffusion and convection, are nearly temperature independent. Gas diffusion may give rise to an arc in the Nyquist plot and the gas diffusion resistance is given by[82]

$$R_{\mathrm{d}} = \left(\frac{\mathrm{R}T}{2\mathrm{F}}\right)^2 \frac{l}{PD_{\mathrm{eff}}} \frac{1}{x_{\mathrm{O}_2}} \tag{4.2}$$

where R is the gas constant, T is the temperature, F is the Faraday constant, P is the pressure, D_{eff} is the effective diffusion coefficient and x_{O_2} is the molar fraction of oxygen.

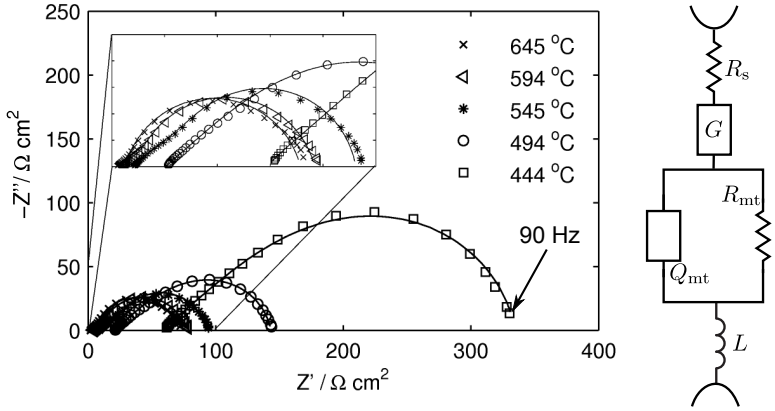

Figure 4.7: Nyquist plot obtained for the impregnated electrode, 4.5, at various temperatures and at an oxygen partial pressure of $5 \cdot 10^{-5}$ bar.

The gas phase mass transport processes are probably related to gas convection and diffusion and were represented by an RQ-circuit, $(R_{\mathrm{mt}}Q_{\mathrm{mt}})$. The exponent n_{mt} was used to take into account the depression of the arc in the Nyquist plot. The impedance of the single phase platinum electrode was therefore fitted with the model $(R_{\mathrm{s}})(L)(R_{\mathrm{e}}Q_{\mathrm{e}})(R_{\mathrm{mt}}Q_{\mathrm{mt}})$ and that of the impregnated electrodes was fitted with the model $(R_{\mathrm{s}})(L)(G)(R_{\mathrm{mt}}Q_{\mathrm{mt}})$. At 744 °C , the addition of CGO20 resulted in a decrease in the polarisation resistance from 62 Ω cm^2 for the single phase platinum electrode to 34 Ω cm^2 for the electrode annealed at 750 °C . R_{mt} was found to be 33 Ω cm^2 and 32 Ω cm^2 for the single phase platinum and the impregnated electrode, respectively. The characteristic frequency of the mass transport processes was found to be $f_{\mathrm{mt}} = 2$ and 4 Hz for the impregnated and the single phase platinum electrode, respectively, and the exponent n_{mt} was found to be between 0.9 and 1.0 for all the electrodes.

At around 500 °C , the addition of CGO20 resulted in a decrease in the polarisation resistance from 656 Ω cm^2 for the single phase platinum electrode to 109 Ω cm^2 for the impregnated electrode annealed at 750 °C (Table 4.4). The addition of CGO20 resulted in a decrease in the characteristic frequency according to Table 4.4. The characteristic frequency of the impregnated electrodes decreased with increasing annealing temperature. The apparent activation energy of R_{e} was found to be 1.0 ± 0.1 eV for the single phase platinum electrode and $1.5 - 1.6$ eV for the impregnated electrodes. The activation energy of R_{CGO} was found to be $0.7 - 0.9$ eV.

Table 4.4: Fitted parameters obtained at around 500 °C and at an oxygen partial pressure of around $5 \cdot 10^{-5}$ bar on the impregnated electrodes, 4.2 to 4.9.

T_A / °C	Pt	750	700	650	600	550
R_s / Ω cm^2	17	22	17	19	17	19
R_p / Ω cm^2	656	109	123	162	164	176
f_e/ Hz	3.1	2.9	2.3	2.2	2.1	2.1

4.5 Discussion

The diameter of the CGO particles observed in the SEM images in Figures 4.1 and 4.2 are in accordance with the grain size obtained from XRD. The difference in the CGO coverage of the platinum surface between the two electrodes shown is probably related to the concentration of surfactant used in the solution. The electrode with the high coverage was impregnated with a solution containing 4 times the amount of surfactant compared with the electrode having a low coverage.

The oxide ion conductivity of nano sized CGO20 grains is almost twice that of CGO10,[68] and this may affect the electrochemical properties. However, a process related to the transport of oxygen ions in the CGO phase was only observed for the CGO20 impregnated electrodes and therefore it is not possible to determine the effect of the difference in ionic conductivity between CGO10 and CGO20. The addition of even a small amount of CGO decreased the polarisation resistance possibly by increasing the TPB length and/or the catalytic activity. The decrease in the polarisation resistance, R_e, with increasing loading showed that there was a loading for which there is no further improvement, around 0.4 mg cm^{-2}. Beyond this, the extra CGO had no significant effect on the polarisation resistance. For small loadings CGO did not affect the capacitance of the Pt/YSZ interface significantly, and it was found to be around 80 μF cm^{-2} (Table 4.2). The impedance spectrum was changed for the impregnated electrodes with a high loading and when the CGO formed a layer on the platinum surface. The impedance was fitted with a Gerischer type impedance and in this model it was assumed that oxygen ions are transported in the CGO phase as illustrated in Figure 4.8. Oxygen may therefore react at the Pt/CGO interface which increases the effective TPB length. The oxygen probably reacts near the Pt/YSZ TPB and therefore a saturation is observed when the extra CGO is deposited outside this region.

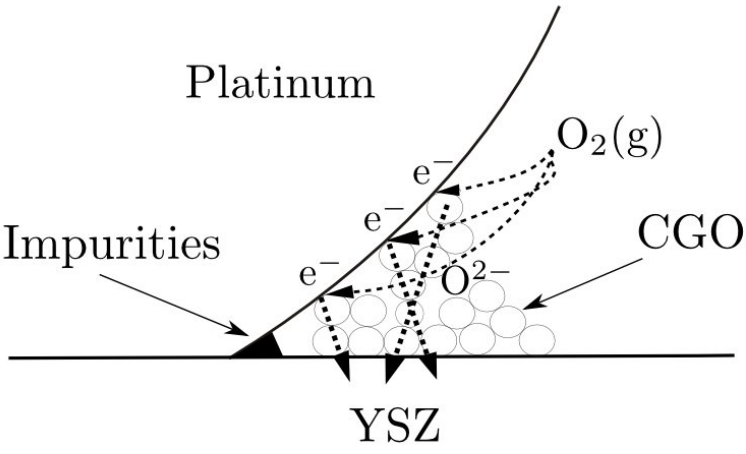

Figure 4.8: Sketch of the interface between a platinum and YSZ grain with impurities blocking the TPB and with CGO grains forming an ionically conducting pathway.

Silicate impurities segregate to the surface during high temperature sintering-Bernasik[83], Hughes and Badwal[84] and are known to inhibit the electrochemical properties of the platinum electrode by blocking the oxygen reaction.[85] If the impurities are deposited at the TPB, as shown in Figure 4.8, they block the oxygen reaction. Impurities might segregate to the CGO grains thereby cleaning the TPB at the Pt/YSZ interface. Due to of the high specific surface area of the CGO grains, the effect might be significant. This may explain the decrease in the polarisation resistance and the increase in the characteristic frequency for small loadings, $< 0.4\,\mathrm{mg\,cm^{-2}}$. But for higher loadings the transport of oxygen ions in the CGO phase was observed to affect the electrochemical properties, as mentioned above.

The impedance obtained from measurements on the electrodes with a high loading were fitted with a Gerischer type impedance as mentioned above. The apparent activation energy of 1.2 ± 0.1 eV for R_{CGO} corresponds to transport of oxygen ions in CGO.[68] The apparent activation energy of the oxygen reaction, R_{e}, was lowered from 2.2 eV for the single phase platinum electrode to $1.2 - 1.5$ eV for the impregnated electrodes, for measurements performed at an oxygen partial pressure of 0.2 bar. The decrease in the apparent activation energy indicated that the oxygen reaction is catalysed by CGO. At low oxygen partial pressures, around $5 \cdot 10^{-5}$ bar, CGO increased the apparent activation

energy from 1 eV for the single phase platinum electrode to $1.5 - 1.6$ eV for the impregnated electrodes. However, CGO reduced the polarisation resistance in the temperature range investigated. The apparent activation energy of R_{CGO} was found to be $0.7 - 0.9$ eV which is slightly lower compared with results obtained at 0.2 bar. The results obtained from fitting at low oxygen partial pressures are affected by the mass transport processes, which may therefore decrease the apparent activation energy.

The polarisation resistance was found to decrease with increasing annealing temperature and increasing CGO grain size. The results were obtained from impregnated electrodes with a high loading and high coverage on the surface of the platinum grains for which the CGO phase facilitate transport of oxygen ions, as mentioned above. The polarisation may therefore decrease if the conductivity of oxygen ions in the CGO phase is increased. Previous investigations have shown that the oxygen ion conductivity of nano sized CGO grains increases with decreasing grain size.[68] However, these results were obtained from measurements on dense samples. The CGO phase obtained from impregnation is porous as shown in Figures 4.1 and 4.2. By increasing the annealing temperature the CGO layer becomes more dense which may therefore enhance the oxygen ion conductivity thereby decreasing the polarisation resistance, as mentioned above. However, there was no correlation between R_{CGO} and the annealing temperature. The impurities also become more mobile at higher temperature which enhances the segregation on the CGO grains. This could increase the effective TPB length at the Pt/YSZ interface, thereby decreasing the polarisation resistance.

For the impregnated electrodes annealed at various temperatures the CGO loading varies between 0.34 and 0.74 mg cm^{-2}. However, there was no correlation between the polarisation resistance and the CGO loading above around 0.4 mg cm^{-2} as mentioned above and the electrodes 4.2 to 4.9 were impregnated following the same approach. The loading of CGO should therefore not influence the observed tendency. The results showed that CGO decreased the polarisation resistance related to the oxygen reaction, which dominated the impedance at temperatures below 496 °C, and at low oxygen partial pressures, around $5 \cdot 10^{-5}$ bar. At similar oxygen partial pressures between 596 and 744 °C, a temperature independent process, related to mass transport by gas diffusion and convection, dominated the impedance. Impregnation with CGO did not affect this process significantly. The results obtained by Gur[86] using cyclic voltammetry also showed that a temperature independent process became rate determining at low oxygen partial pressures and high temperatures.

4.6 Conclusion

The polarisation resistance of porous platinum electrodes was decreased by up to an order of magnitude by impregnation with CGO. For high loadings a porous layer of CGO was formed on the surface of the platinum grains, which facilitated transport of oxide ions thereby increasing the effective TPB length. Above a CGO loading of 0.4 mg/cm^2 there was no correlation between the polarisation resistance and the CGO loading. The polarisation resistance of the CGO impregnated electrodes was found to decrease with increasing annealing temperature which is interpreted as due to an increased oxide ion conductivity of the CGO phase. The increased TPB length would make the platinum electrode more robust and tolerant to poisoning. CGO was found to decrease the apparent activation energy of the oxygen reaction at an oxygen partial pressure of 0.2 bar and increase it at an oxygen partial pressure of $5 \cdot 10^{-5}$ bar. Gas phase mass transport processes became dominating above 600 °C at an oxygen partial pressure of 10^{-5} bar. The addition of CGO did not have any significant effect on the mass transport processes.

4.7 Acknowledgements

This work was supported financially by The Programme Commission on Sustainable Energy and Environment, The Danish Council for Strategic Research, via the Strategic Electrochemistry Research Center (SERC) (www.serc.dk), contract no. 2104-06-0011.

CHAPTER 5

Limitations of potentiometric oxygen sensors

This chapter was submitted as A. Lund, T. Jacobsen, K. V. Hansen, M. Mogensen, "Limitations of potentiometric oxygen sensors operating at low oxygen levels ", Sensors and Actuators B: Chemical

5.1 Abstract

The electrochemical processes that limit the range of oxygen partial pressures in which potentiometric oxygen sensors can be used, were analysed using a theoretical and an experimental approach. Electrochemical impedance spectroscopy was performed on porous Pt/yttria stabilised zirconia (YSZ) electrodes between 10^{-6} and 0.2 bar and at temperatures between 500 and 950 °C.

The flow of oxide ions and electron holes through a sensor cell, with a YSZ electrolyte, were calculated under similar conditions. The oxygen permeation of the sensor cell was insignificant at an oxygen partial pressure of 10^{-6} bar for an inlet flow rate higher than 2 L h^{-1} between 600 and 800 °C. The polarisation resistance measured between 10^{-6} and 10^{-4} bar was found to be inversely proportional to the oxygen partial pressure, nearly temperature independent and inversely proportional to the inlet gas flow rate, which shows that gas phase mass transport processes were dominating. The time constant of the gas phase mass transport processes was found to be inversely proportional to the oxygen partial pressure. The response time of these processes therefore limits the oxygen partial pressure range in which potentiometric oxygen sensors can be used.

5.2 Introduction

The processes that limit the oxygen partial pressure range that can be monitored with yttria stabilised zirconia (YSZ) based potentiometric oxygen sensors are not well described. Problems with the measurement of the oxygen partial pressure around 10^{-6} bar mainly originate from the slow sensor response[13,17–19]. Furthermore, oxygen leakages and the oxygen permeability of the YSZ electrolyte may change the oxygen partial pressure. However, knowing which parameters are limiting, the sensor may be improved to operate at even lower oxygen partial pressures which is relevant in for example the development of potentiometric sensors for sub-ppm level detection of gaseous species[87].

The potentiometric oxygen sensor is applied in for example the industrial food preservation and typically operates at oxygen partial pressures of $10^{-4} - 10^{-6}$ bar in gaseous nitrogen. It consist of a cell with two porous electrodes separated by a dense electrolyte[23,39]. One of the electrodes is used as a reference and senses a constant oxygen partial pressure, for example that of air or that of an internal oxygen reference[11]. The most commonly used electrode material in oxygen sensors is platinum with YSZ as the electrolyte[3,12]. Below 500 ^{o}C the response time of the platinum electrode becomes too long[27], and therefore oxygen sensors typically operate around 700 ^{o}C. The oxygen sensors may be designed in several ways[19], but in the following we consider only the most often used which has a closed-end tube. For this type of geometry the electrode is covered by a stagnant gas layer, which forms a diffusion barrier, and

a continuously stirred layer[60]. The gas transport across these layers is therefore given by diffusion and convection. The processes may be characterised by performing electrochemical impedance spectroscopy (EIS) measurements in a broad range of frequencies in which the electrode processes may be separated by their characteristic frequencies. The polarisation resistance related to gas diffusion and convection is inversely proportional to the oxygen partial pressure[60,82] and may therefore determine the response time at low oxygen partial pressures. Furthermore, the electron hole conductivity of the YSZ[88] leads to a small error in the measured potential and also causes a small leakage of oxygen through the sensor cell[26].

The influence of the oxygen permeation of the YSZ and the gas transport processes on the measured oxygen partial pressure and the response time are therefore investigated. In the following we investigate the electrochemical properties of a porous Pt/YSZ cermet electrode by EIS at various oxygen partial pressures ranging from near 10^{-6} bar to atmospheric air, at inlet gas flow rates between 4 and 12 L h^{-1} and at temperatures between 500 and 950 °C to study how the mass transport processes influence the response time. We also model the error introduced by the small electron hole conductivity of the YSZ to know how it influences the measurement of the oxygen partial pressure.

5.3 Theory

5.3.1 The influence of the oxygen permeation on the measured oxygen partial pressure

Figure 5.1a shows the cross section of an oxygen sensor cell. The cell generates an electromotive force, E_{eq}, given by the difference in oxygen partial pressure between the process gas and air, which is used as a reference gas. The process gas flows towards the working electrode inside an alumina tube while the reference electrode is placed in air. Figure 5.1b shows the corresponding equivalent circuit. The YSZ has, besides a high ionic conductivity, also semiconductor properties. The small electron hole conductivity gives rise to a small flow of oxide ions, $J_{YSZ,O}$, and electron holes, $J_{YSZ,h}$, through the YSZ electrolyte from the reference to the working electrode, depending on the difference in oxygen partial pressure. The flow of electron holes is considerably higher than the flow of electrons at oxygen partial pressures above 10^{-6} [88]. Therefore, only

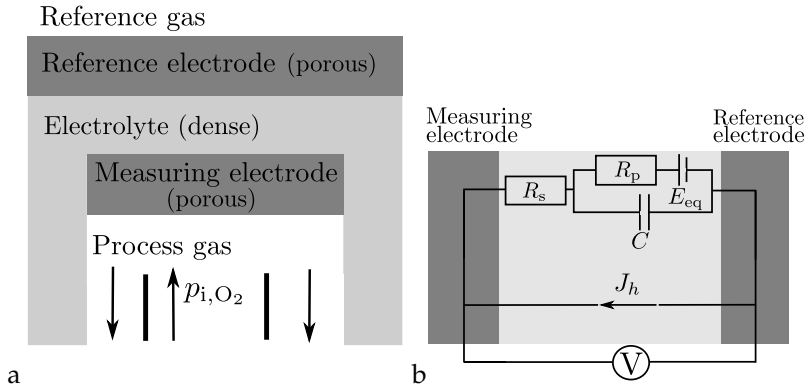

Figure 5.1: a. Cross section of a sensor cell. b. equivalent circuit of the sensor cell.

the flow of electron holes is considered here to simplify the calculation. The oxygen reaction including mass transport processes is represented by an *RC*-circuit. R_p is the polarisation resistance and C is the capacitance. The ohmic loss associated with the transport of oxide ions through the YSZ is represented by a resistor, R_s. The actual potential between the reference electrode and the working electrode in the steady state is therefore given by

$$E = E_{eq} - iR_s - iR_p. \tag{5.1}$$

where i is the current density. The deviation of the measured potential from the Nernst potential is then given by

$$\Delta E = E - E_{eq} = \mathrm{F} J_{YSZ,h}(R_p + R_s) \tag{5.2}$$

where F is Faraday's constant. The polarisation resistance depends on the given electrode and should therefore be determined experimentally to calculate the deviation from the Nernst potential. In a later section the polarisation resistance is obtained from EIS measurements.

The flow of electron holes through the YSZ electrolyte increases the oxygen partial pressure at the working electrode. In the steady state the actual oxygen partial pressure is therefore given by

$$p_{O_2} = \frac{J_{i,O_2} + J_{YSZ,O}}{J_i + J_{YSZ,O}} P \approx \frac{J_{i,O_2} + J_{YSZ,O}}{J_i} P \tag{5.3}$$

where P is the atmospheric pressure, J_i is the inlet gas flow and J_{i,O_2} is the inlet oxygen flow which is given by

$$J_{i,O_2} = J_i \frac{p_{i,O_2}}{P} \tag{5.4}$$

where p_{i,O_2} is the oxygen partial pressure of the inlet gas. The flow of oxygen through the YSZ electrolyte, due to the flow of oxide ions and electron holes, can be calculated from the flow of electron holes as

$$J_{YSZ,O} = \frac{J_{YSZ,h}}{4}. \tag{5.5}$$

Assuming that the electron hole diffusion coefficient, D_h, is constant and the electron hole concentration varies linearly through the YSZ, the flow of electron holes through the YSZ can be calculated according to Fick's law as

$$J_{YSZ,h} = -D_h \frac{c_{h,g} - c_{h,a}}{\delta_{YSZ}} \tag{5.6}$$

where δ_{YSZ} is the thickness of the electrolyte, D_h is the electron hole diffusion coefficient and $c_{h,g}$ and $c_{h,a}$ are the electron hole concentration of the YSZ in the process gas and in air, respectively. The electron hole concentration and diffusion coefficient in the YSZ electrolyte was calculated according to Park and Blumenthal[88] where the value of the electron hole diffusion coefficient was calculated as $D_h = 0.23 \exp(-1.15\ \mathrm{eV}/k_B T)$. The electron hole concentration was calculated as $c_h = 1.72 \times 10^{21} \exp(-0.62\ \mathrm{eV}/k_B T) p_{O_2}^{1/4}$ assuming that there is equilibrium between the oxygen activity in the oxide and the oxygen content in the gas, where k_B is the Boltzmann constant. The relative deviation between the measured oxygen partial pressure and that of the inlet gas, $\Delta p_{O_2}/p_{i,O_2} = (p_{O_2} - p_{i,O_2})/p_{i,O_2}$, is shown in Figure 5.2. It is seen that the deviation in the oxygen partial pressure increases with increasing temperature and decreasing flow rate. The flow of oxygen through the YSZ was calculated using an electrolyte thickness $\delta_{YSZ} = 0.2$ cm and an inlet oxygen partial pressure $p_{i,O_2} = 10^{-6}$ bar. It is seen that the difference is less than 10% when then gas flow per unit area is higher than 2 L $h^{-1}cm^{-2}$ and the temperature is between 600 and 800 °C.

5.3.2 The response time and the gas phase mass transport processes

In Figure 5.1, the processes related to the oxygen reaction and gas phase mass transport were represented by an *RC*-circuit. The response to a given change in the oxygen partial pressure is therefore a function of time and determines the time needed for a measurement of the oxygen partial pressure. For a change in the oxygen partial pressure the change in the measured potential may be ex-

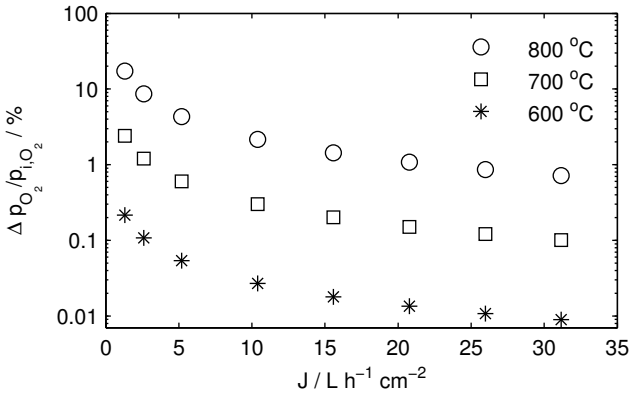

Figure 5.2: The relative deviation in the oxygen partial pressure as a function of the inlet nitrogen gas flow rate per unit electrode area at around 20 °C with $p_{\mathrm{i,O_2}} = 10^{-6}$ bar at various temperatures.

pressed as a sum of exponentially decaying functions of time like for example

$$\Delta E_{measured} = \sum_{\mathrm{i}} \Delta E_{\mathrm{i}} \mathrm{e}^{-t/\tau_{\mathrm{i}}} \tag{5.7}$$

where τ_i is a time constant and ΔE_{i} is the potential difference of process i and t is the time. The time constant, $\tau_{\mathrm{i}} = R_{\mathrm{i}} C_{\mathrm{i}}$, can be calculated if the polarisation resistance and the capacitance of the processes are known.

Figure 5.3 shows a cross section of the sensor cell and a model of the oxygen transport in the stagnant gas layer over the working electrode. The x-axis is parallel to the surface of the electrode and the y-axis is parallel to the surface normal. The stagnant gas layer is assumed to consist of a diffusion layer with thickness δ_{D} and a continuously stirred layer with thickness δ_{g} and volume V. In the top part of the figure the gas first enters the stagnant gas layer through the inlet tube. The inlet and outlet oxygen partial pressures and velocities are represented by $p_{\mathrm{i,O_2}}$, v_{i} and $p_{\mathrm{o,O_2}}$, v_{o}, respectively. J_* is the flow of oxygen at the surface of the working electrode, $y = 0$, which for an AC measurement is given by $J_* = i_0 \mathrm{e}^{i\omega t}/4\mathrm{F}$. i_0 is the amplitude of the AC current, ω is the angular frequency and t is the time. The continuously stirred layer is assumed to be perfectly mixed. The change in oxygen partial pressure in the continuously stirred volume is given by

$$\delta_{\mathrm{g}} \frac{1}{\mathrm{R}T} \frac{\partial p_{\mathrm{O_2}}}{\partial t} = \frac{1}{\mathrm{R}T} v_{\mathrm{i}} p_{\mathrm{i,O_2}} - \frac{1}{\mathrm{R}T} v_{\mathrm{o}} p_{\mathrm{o,O_2}} + J_{\mathrm{D}} \tag{5.8}$$

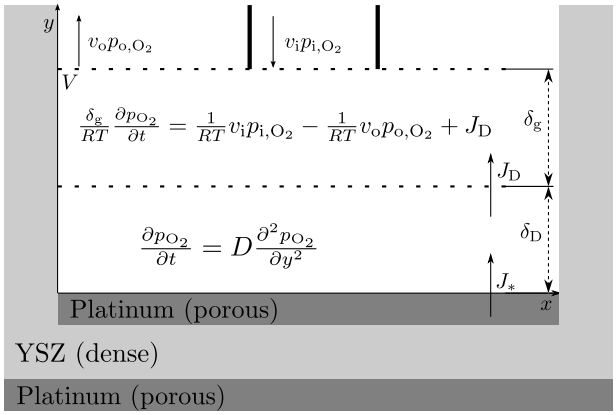

Figure 5.3: A cross section of the sensor cell with a model of the oxygen transport in the stagnant gas layer which is divided into two parts, a gas diffusion layer and a continuously stirred layer. The inlet and outlet oxygen partial pressures and velocities are represented by p_{i,O_2}, v_i and p_{o,O_2}, v_o, respectively. The x-axis is parallel to the surface of the electrode and the y-axis is parallel to the surface normal.

where J_D is the flow of oxygen from the diffusion layer, for $y = \delta_D$. The change in the oxygen partial pressure of the diffusion layer can be calculated according to the diffusion equation as

$$\frac{\partial p_{O_2}}{\partial t} = D\frac{\partial^2 p_{O_2}}{\partial y^2} \tag{5.9}$$

where D is the effective binary gas diffusion coefficient. By solving the two coupled differential equations, 5.8 and 5.9, the corresponding impedance can be calculated according to Jacobsen *et al.* [60], to be

$$Z_{mt} = \frac{Z_D + Z_C}{1 + \frac{Z_C}{R_D}\sqrt{\tau_D i\omega}\tanh[\sqrt{\tau_D i\omega}]} \tag{5.10}$$

where the diffusion impedance, Z_D, and the conversion impedance, Z_C are inversely proportional to the oxygen partial pressure. ω is the angular frequency. The part related to gas diffusion is similar to the impedance of a finite-length Warburg impedance element

$$Z_D = \frac{R_D}{\sqrt{\tau_D i\omega}}\tanh[\sqrt{\tau_D i\omega}] \tag{5.11}$$

where the gas diffusion time constant is given by $\tau_D = \delta_D^2/D$ and $R_D \propto \delta_D$.

The gas conversion impedance can be represented by an *RC*-circuit

$$Z_C = \frac{1}{i\omega C_C + \frac{1}{R_C}} \tag{5.12}$$

where the gas conversion resistance, R_C, is inversely proportional to the inlet gas flow and the capacitance, C_C, is proportional to the volume of the continuously stirred layer, V [60].The time constant of the gas conversion process can then be calculated as $\tau_C = R_C C_C$ and it is inversely proportional to the inlet gas flow, J_i and proportional to the volume, V, and independent of the oxygen partial pressure

$$\tau_C \propto \frac{V}{J_i}. \tag{5.13}$$

Decreasing the stagnant gas layer volume and increasing the inlet gas flow rate therefore decreases the response time. For example for a volume, $V = 0.5$ cm^3, an electrode area, $A = 1$ cm^2 and an inlet gas flow, $J_i = 8$ L h^{-1} cm^{-2} at 700 ^{o}C, the time constant is $\tau_C = 0.23$ s, using that $\tau_C = \frac{PV}{J_i ART}$ [89].

5.4 Experimental

A paste of platinum (Engelhard, No: 6082A) mixed with 8 mol% YSZ (99.85%, Tosoh Corp.) with a volume ratio between platinum and YSZ of 1:1 was brush painted on a 3-electrode pellet[?] of 8 mol% YSZ (99.85 %, Tosoh Corp.) to produce a working electrode with an area of 0.39 cm^2. The 3-electrode pellet was painted four times and then sintered at 1200 °C in air for 2 h to produce a porous working electrode. The counter and reference electrodes were painted once on the 3-electrode pellet using a platinum paste that did not contain YSZ and then sintered at 1000 °C for 2 h.

Figure 5.4 shows a cross section of the test setup and the 3-electrode pellet of YSZ. The working electrode was placed in a controlled atmosphere of mixed dry N_2 and air. The oxygen partial pressure was controlled between 0.2 bar and 10^{-6} bar, with an accuracy of ±10%, by mixing these gasses or supplying oxygen into streaming N_2 by an electrochemical pumping cell. The oxygen partial pressure at the counter and reference electrode was 0.2 bar. The inlet gas flow rate was between 4 and 15 L h^{-1}. The oxygen partial pressure at the working electrode was monitored by measuring the potential difference between the working and the reference electrode and the temperature, which

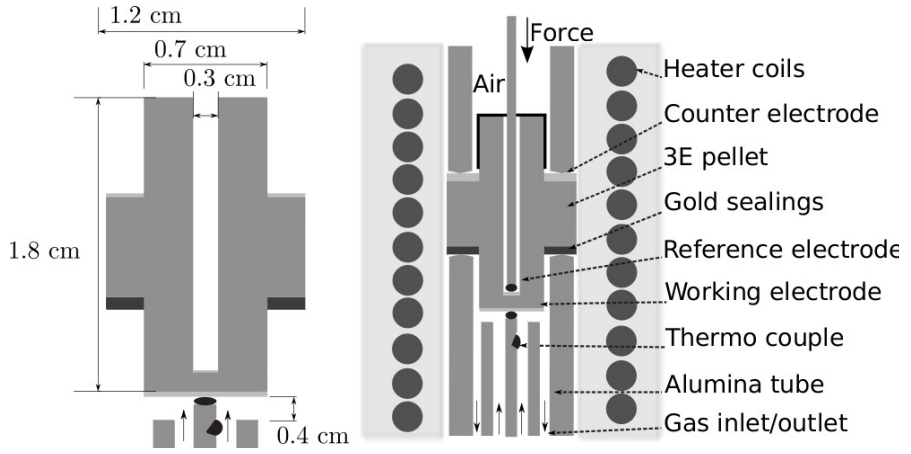

Figure 5.4: A drawing showing the cross section of the test setup.

was controlled with an accuracy of $\pm 1\ ^{o}$C. Furthermore, a potentiometric oxygen sensor was used to measure the oxygen partial pressure of the gas outlet.

5.4.1 Electrode microstructure

SEM images of the electrode were obtained using field emission SEM (Zeiss SUPRA-35) with a secondary electron (SE) detector. Figure 5.5 shows an SEM image of a part of the electrode, which has been fractured. The agglomerated Pt particles are around 2 µm in diameter while the agglomerated YSZ particles are around 0.2 µm. The thickness of the electrode was determined to be approximately 13 µm from an image taken of a part of the electrode cross section.

5.4.2 Electrochemical impedance spectroscopy measurements

EIS measurements were performed with a Solartron 1255 frequency response analyser and a Solartron 1287 potentiostat in a frequency range from 10 kHz to 2 mHz with 3 to 20 measurements per frequency decade at open circuit voltage

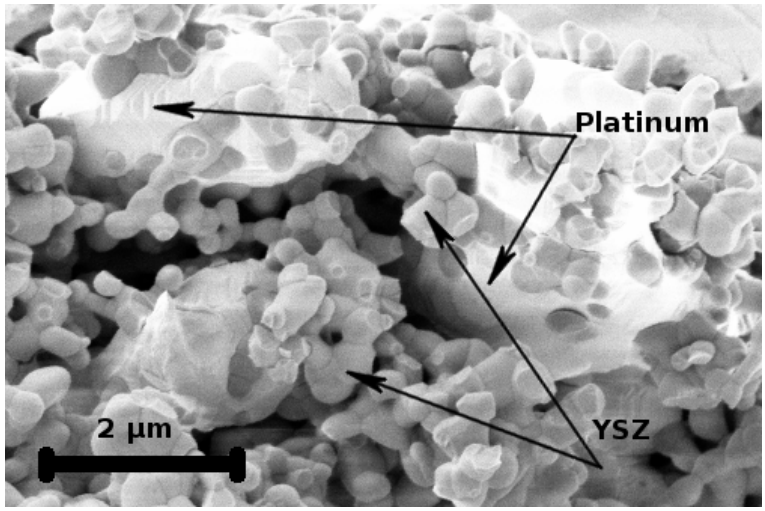

Figure 5.5: A scanning electron micrograph (SE detector) of the porous Pt/YSZ working electrode.

with an AC root mean square amplitude of 0.5 mV. The measurements were performed between 500 and 950 °C and between an oxygen partial pressure of 10^{-6} and 0.2 bar. The EIS data were fitted with equivalent circuit models using the Levenberg–Marquardt algorithm in Matlab.

$p_{O_2} > 10^{-3}$ bar

Figure 5.6 shows the Nyquist plot for measurements performed between 4.4×10^{-3} and 0.1 bar. It is seen that the polarisation resistance of the low frequency arc increases only slightly with decreasing oxygen partial pressure indicating that the mass transfer processes are of minor importance in this range of oxygen partial pressures. The polarisation resistance of the high frequency arc is independent of the oxygen partial pressure.

The impedance was fitted with the equivalent circuit model $(R_s)(L)(R_{e1}Q_{e1})(R_{e2}Q_{e2})$, where the series resistance, R_s, is connected in series with an inductance element L, and two RQ-circuits. The series resistance includes the resistance of the wires and the ohmic loss due to transport of oxide ions in the YSZ electrolyte. The inductance element is included to take into account high frequency induc-

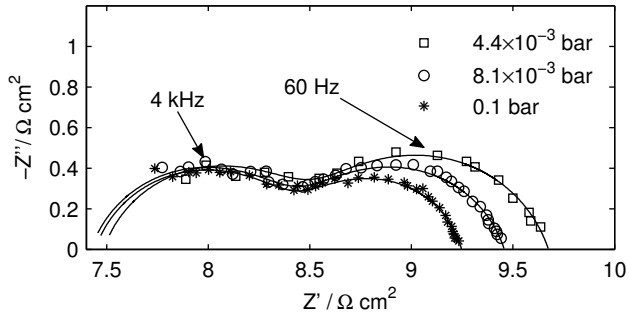

Figure 5.6: Nyquist plot obtained at various oxygen partial pressures at 700 ^{o}C and an inlet gas flow rate of 8 L h^{-1}.

tance and instrumental artefacts. Each of the RQ-circuits consists of a resistor, R and a constant phase element, Q which is connected in parallel. e1 and e2 represent the high and low frequency electrode processes, respectively. The depression of the arcs, given by the parameter n of the constant phase element, was fixed to 0.8 for Q_{e1} and Q_{e2} to decrease the number of free parameters. Apparent activation energies of 1.2 ± 0.2 eV and 1.9 ± 0.2 eV were found for R_{e1} and R_{e2}, respectively, for measurements performed at 0.2 bar between 650 and 950 °C. The apparent activation energy of the electrolyte resistance was found to be 0.88 ± 0.04 eV between 500 and 850 °C which is in agreement with results previously obtained by Badwal [80].

$p_{O_2} < 10^{-3}$ bar

The Nyquist plot in Figure 5.7 shows that one arc with a peak frequency of 0.1 Hz at 1.2×10^{-6} bar dominates the impedance spectrum. At 49×10^{-6} bar, the peak frequency of the dominating arc is 1.9 Hz. The impedance is seen to be much more dependent on the oxygen partial pressure compared with the impedance measured above 10^{-3} bar. The dominating arc may therefore represent mass transport processes such as gas diffusion and convection. The impedance spectra obtained were therefore fitted with an equivalent circuit model similar to the one used above, but connected in series with an element that represents the mass transport processes. The diffusion resistance could not be identified when fitting the arc related to the mass transport processes with the impedance given in Equation 5.10. A simplified model, consisting of an

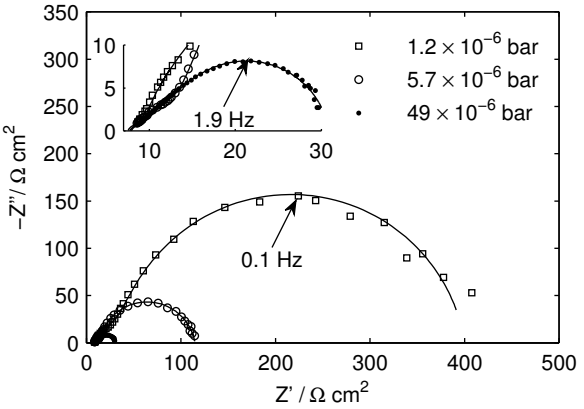

Figure 5.7: Nyquist plot obtained at various oxygen partial pressures at 700 ^{o}C and an inlet gas flow rate of 8 L h^{-1}.

RQ-circuit, was therefore used to represent the mass transport processes and the fits are shown in Figure 5.7. The frequency term was corrected by an exponent, $(i\omega)^{n_{mt}}$, to take into account the depression of the arc. The exponent was fixed to 0.9 to decrease the number of free parameters. R_{mt} is the polarisation resistance related to mass transport processes. The polarisation resistance R_{mt} did not change significantly with temperature for measurements performed at 5.7×10^{-6} bar between 650 and 950 °C, thus confirming the contribution as due to mass transfer. It was not possible to separate the contribution from R_{e1} and R_{e2} at an oxygen partial pressure of 5.7×10^{-6} bar to calculate separate activation energies. The apparent activation energy for $R_{\mathrm{e1}} + R_{\mathrm{e2}}$ was found to be 0.8 $\pm$ 0.1 eV for measurements performed between 500 and 750 °C. The lowest oxygen partial pressure measured was 1.3×10^{-6} bar. The potential between the working and the reference electrode was found to be 0.249 V, while the potential across the cell of the outlet sensor was 0.252 V, at 700 °C. The difference in the measured potential corresponds to a difference of only $\Delta p_{\mathrm{O_2}} = 10^{-7}$ bar and may be caused by temperature gradients between the working and the reference electrode of the 3-electrode setup or the external oxygen sensor. The small potential difference is taken as confirmation of a fairly gas tight experimental setup.

Figure 5.8 shows that the overall polarisation resistance $R_{\mathrm{p}} = R_{\mathrm{e1}} + R_{\mathrm{e2}} + R_{\mathrm{mt}}$ increases with decreasing oxygen partial pressure. The polarisation resistances R_{mt} and R_{e2} were fitted with a function of the form $R = A p_{\mathrm{O_2}}^{-m}$ to obtain the oxygen partial pressure dependencies. The polarisation resistance R_{mt} was found to be inversely proportional to the oxygen partial pressure,

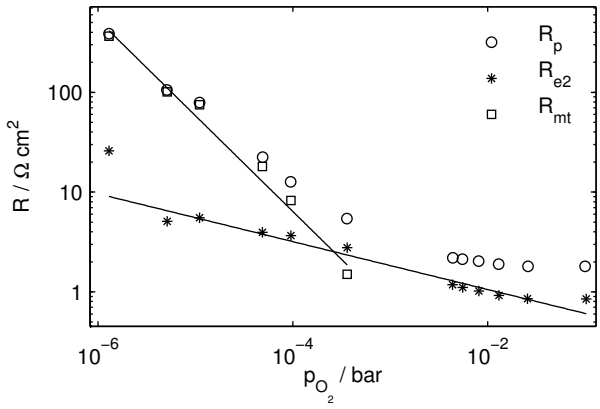

Figure 5.8: The polarisation resistance as a function of the oxygen partial pressure at 700 ^{o}C and at an inlet gas flow rate of 8 L h^{-1}.

$m = 1.0 \pm 0.1$, and for R_{e2} the exponent, m, was found to be 0.24 ± 0.03. Below 10^{-3} bar, the slope of R_p versus p_{O_2} changes because the mass transport processes dominates the polarisation resistance, whereas the electrode reaction dominates above 10^{-3} bar.

Figure 5.9 shows that the capacitance, C_{mt}, of the mass transport process does not depend on the oxygen partial pressure below 10^{-4} bar. The time constant, $\tau_{mt} = R_{mt}C_{mt}$, is therefore inversely proportional to the oxygen partial pressure. This tendency is not in accordance with the model of the stagnant gas layer, because the time constants of the gas diffusion and conversion impedances are independent of the oxygen partial pressure.

The influence of the inlet gas flow rate

The impedance spectra were measured at various inlet gas flow rates at constant temperature and oxygen partial pressure. At 700 ^{o}C and an oxygen partial pressure of 3.6×10^{-4} bar, three arcs were identified from the Nyquist plot in Figure 5.10. It is seen that the polarisation resistance increases with decreasing gas flow rate, which is mainly due to an increase of the arc with a peak frequency of 2 Hz. The fits are shown with a solid line using the same model as before for measurements performed at low oxygen partial pressures.

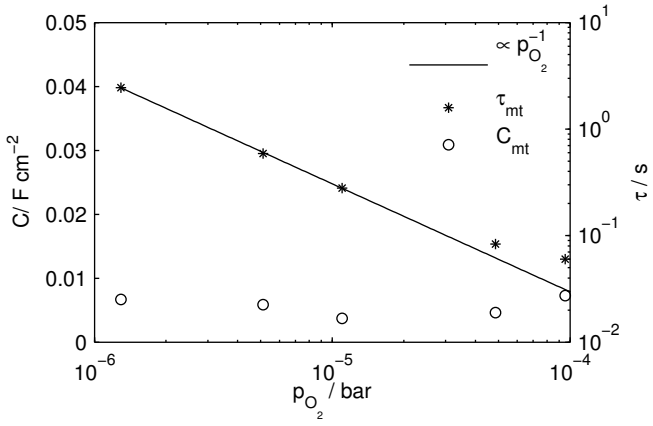

Figure 5.9: The characteristic frequency and the capacitance of the mass transport process as functions of the oxygen partial pressure for measurements performed at 700 °C and at an inlet gas flow rate of 8 L h^{-1}.

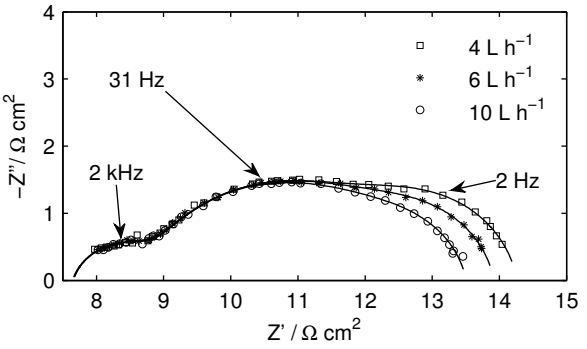

Figure 5.10: Nyquist plot obtained at 700 °C at an oxygen partial pressure of 3.6×10^{-4} bar for various gas flow rates.

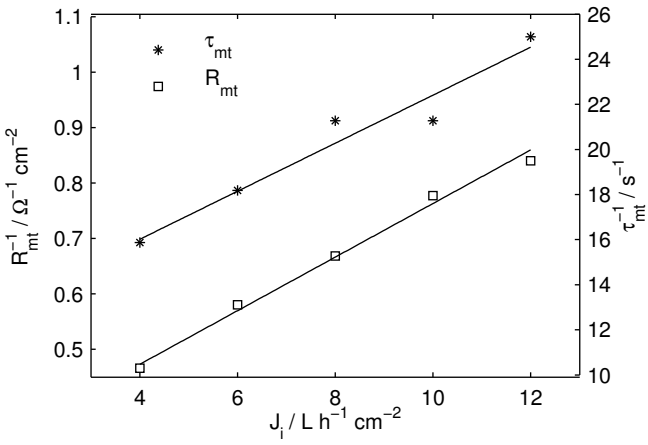

Figure 5.11: The inverse polarisation resistance, R_{mt}^{-1}, and the inverse time constant, τ_{mt}^{-1}, as functions of the inlet gas flow rate per unit area at 700 ^{o}C and at an oxygen partial pressure of 3.6×10^{-4} bar.

Figure 5.11 shows that the polarisation resistance, R_{mt}, and the time constant, τ_{mt}, are inversely proportional to the inlet gas flow rate in accordance with the model of the stagnant gas layer. However, the calculated volume was found to increase from 0.2 to 0.4 cm^3 assuming that the time constant of the gas conversion process is equal to $\tau_{\mathrm{C}} = \tau_{\mathrm{mt}}$ and that $\tau_{\mathrm{C}} = \frac{PV}{J_i ART}$ [89]. In the model of the stagnant gas layer the volume is assumed to be constant, which shows that there is a discrepancy between the model and the measured impedance.

5.5 Discussion

It can be shown that the polarisation resistance at the equilibrium potential is proportional to $p_{\mathrm{O_2}}^{-0.25}$ at low oxygen partial pressures if the reaction order, with respect to the oxygen partial pressure, is 0.5 [44,90,91]. The polarisation resistance, R_{e2}, was found to be proportional to $p_{\mathrm{o_2}}^{-0.24}$ and to have an activation energy of 1.9 eV for EIS measurements performed at 0.2 bar and 0.8 eV at 5.7×10^{-6} bar. The apparent activation energies are in agreement with values previously found for the oxygen reaction at the Pt electrode [75,91]. This process is therefore related to the oxygen charge transfer reaction. The high frequency arc, with

the polarisation resistance R_{e1}, was found to be independent of the oxygen partial pressure and to have an activation energy of 1.2 eV for measurements performed at 0.2 bar oxygen. The activation energy is similar to that of the bulk oxide ion conductivity of YSZ[80] and R_{e1} may therefore be related to transport of oxide ions in the electrode YSZ phase.

Between 10^{-4} and 10^{-6} bar, the low frequency polarisation resistance, R_{mt}, is dominant, and was found to be inversely proportional to the oxygen partial pressure and nearly temperature independent, which indicates that it is related to gas phase mass transport. Only the mass transport process related to gas conversion could be identified from the impedance spectra. The gas conversion resistance can be calculated as $R_C = \frac{PRT}{16F^2}\frac{1}{J_i}\frac{1}{p_{i,O_2}}$,[89] where P is the atmospheric pressure. At 700 °C, an oxygen partial pressure of 3.6×10^{-4} bar and an inlet flow of 8 L h^{-1} cm^{-2} at 25 °C, the gas conversion resistance was calculated to be 0.58 Ω cm^2. The measured polarisation resistance related to the mass transport processes, R_{mt}, was 1.5 Ω cm^2 which indicates that only a part of the inlet gas stream is used, as expected. It is likely that both diffusion and conversion contribute to the mass transport processes and the impedance of these is inversely proportional to the oxygen partial pressure. However, the diffusion processes could not be identified because the diffusion boundary length was either very short compared with the thickness of the continuously stirred layer, or the diffusion process is more complex than that of a stagnant diffusion layer.

The measured mass transport time constant is inversely proportional to and the capacitance is independent of the oxygen partial pressure between 10^{-6} and 10^{-4} bar, which cannot be accounted for by mass transport in a continuously stirred layer and a diffusion layer. The results indicate that the response time for an oxygen sensor is inversely proportional to the oxygen partial pressure below 10^{-3} bar. At 700 ^{o}C, the characteristic frequency was found to be 0.1 and 0.28 Hz at oxygen partial pressures of 1.2×10^{-6} and 5.7×10^{-6} bar, respectively. This corresponds to volumes of 22 and 4.2 cm^3, respectively, using that $f_{mt} = \frac{1}{2\pi\tau_C} = \frac{J_i RT}{2\pi PV}$.[89] However, the volume of the sensor tubes is around 10 cm^3. At 3.6×10^{-4} bar, the calculated volume was found to increase from around 0.2 to 0.4 cm^3 when increasing the inlet gas flow rate from 4 to 12 L h^{-1}. The volume should not depend on the oxygen partial pressure and the inlet gas flow rate. The model of the mass transport processes cannot account for the very large and constant capacitance of 0.01 F cm^{-2}. The oxygen reaction probably takes place near the electrode/electrolyte interface due to the ionic resistance of the electrode YSZ phase. Therefore a part of the YSZ phase is inactive and stores oxygen due to changes in stoichiometry. The differential

capacitance related to the changes in the stoichiometry of the electrode YSZ phase is

$$C = \frac{dQ}{dE} = V_{\mathrm{YSZ}}\mathrm{F}\frac{d[\mathrm{h}^{\cdot}]}{dE} \tag{5.14}$$

where V_{YSZ} is the volume of the electrode YSZ phase and $[\mathrm{h}^{\cdot}]$ is the concentration of electron holes in the electrode YSZ phase. The concentration can be calculated according to Park and Blumenthal[88] as previously mentioned. Assuming that there is equilibrium then $dE = \frac{\mathrm{R}T}{4\mathrm{F}}\frac{1}{p_{\mathrm{O_2}}}dp_{\mathrm{O_2}}$. The thickness of the electrode is around 13 μm, the area is 0.39 cm^2 and the fraction of YSZ in the electrode is around 0.25 which gives a maximum differential capacitance of 104 $\mu\mathrm{F\,cm}^{-2}$. The stoichiometric changes in the YSZ therefore cannot account for the measured capacitance. It shows that the mass transport processes are probably more complex than what can be accounted for using the model presented here.

If there was a diffusion barrier, it would in principle give rise to a gradient in the oxygen partial pressure at the working electrode because of the flow of oxide ions and electron holes through the YSZ electrolyte. The difference in the oxygen partial pressure across this barrier can be calculated according to Fick's first law as

$$\Delta p_{\mathrm{O_2}} = \frac{J_{\mathrm{YSZ,O}}\mathrm{R}T}{D_{12}}\frac{\gamma}{\epsilon}\delta_{\mathrm{D}} \tag{5.15}$$

where $D_{12} = 1.6\ \mathrm{cm}^2\ \mathrm{s}^{-1}$ is the binary diffusion coefficient at 700 °C and $J_{\mathrm{YSZ,O}}$ can be calculated according to Equations 5.5 and 5.6[92]. The microstructure of the electrode can be accounted for by multiplying the binary diffusion coefficient with a porosity, ϵ, and dividing with a tortuosity factor, γ. Increasing the porosity and decreasing the tortuosity decreases the difference in the oxygen partial pressure. At an oxygen partial pressure of 10^{-6} bar at 700 ^{o}C, the flow of oxide ions through the YSZ electrolyte with a thickness 0.2 cm was calculated to be 3.6×10^{-13} mole $\mathrm{s}^{-1}\ \mathrm{cm}^{-2}$. The difference is then negligible, 10^{-9} bar, for a diffusion boundary length of $\delta_{\mathrm{D}} = 100$ μm and assuming that the porosity is 0.5 and the tortuosity factor is, $\gamma = 3$, because the electrode is porous and the path through the electrode is therefore slightly longer than the thickness of the electrode.

The deviation due to the flow of oxide ions and electron holes through the YSZ electrolyte increases proportionally to the active area. The area covered by platinum is active but oxygen may in principle also react at the YSZ surface. The surface exchange flow across the YSZ/gas interface at equilibrium can be calculated as $J_{0,\mathrm{O}} = k_{\mathrm{c}}[\mathrm{O}^{2-}]$.[93] The surface exchange coefficient, k_{c}, was measured by Manning *et al.*[94] in pure oxygen at 700 °C to be 5.0×10^{-9} cm s^{-1}

and the concentration of the oxide ions in YSZ (cubic-fluorite structure) is approximately 0.1 mole cm^{-3}. The surface exchange coefficient is proportional to $p_{O_2}^{0.25}$.[95] At an oxygen partial pressure of 10^{-6} bar, the exchange flow can then be calculated to be $J_{0,O} = 1.6 \times 10^{-11}$ mole s^{-1} cm^{-2}. This corresponds to a DC resistance of $R = \frac{1}{2FJ_{0,O}} \frac{RT}{4F} = 6.9$ kΩ cm^2, at 700 °C. This resistance is much higher compared with the polarisation resistance of the oxygen reaction at the platinum electrode. However, the oxide ion exchange flow is high compared with the permeation of oxide ions through the YSZ, which is 3.6×10^{-13} mole s^{-1} cm^{-2} at similar conditions. This indicates, that the oxygen permeation is not confined to the electrode area.

The change in oxygen partial pressure, Δp_{O_2}, due to the permeation of oxide ions and electron holes through the 3-electrode pellet can be calculated according to Equations 5.3 and 5.4 as

$$\Delta p_{O_2} = p_{O_2} - p_{i,O_2} = \frac{J_{YSZ,O}}{J_i} P = 6 \times 10^{-9} \text{ bar} \tag{5.16}$$

at an oxygen partial pressure of 10^{-6} bar at 700 °C and an inlet flow rate of 8 L h^{-1}. The area of the 3-electrode which is exposed to the gas is $A = \pi \times 0.35^2$ $cm^2 + 2 \times \pi \times 0.35 \times 0.4$ $cm^2 = 1.3$ cm^2, which gives an inlet gas flow per unit area of 6.2 L h^{-1} cm^{-2}. This shows that the contribution from the oxide ion permeation through the 3-electrode pellet is insignificant. The potential drop associated with the change in oxygen partial pressure can be calculated to be

$$\Delta E = \frac{RT}{4F} \ln\left(\frac{p_{i,O_2} + \Delta p_{O_2}}{p_{i,O_2}}\right) \approx \frac{RT}{4F} \frac{\Delta p_{O_2}}{p_{i,O_2}} = \frac{RTP}{4F} \frac{1}{J_i} \frac{1}{p_{i,O_2}} J_{YSZ,O} = 1.1 \times 10^{-4} \text{ V} \tag{5.17}$$

The change in potential is equivalent to the potential drop of the gas conversion resistance, $R_C = \frac{PRT}{16F^2} \frac{1}{J_i} \frac{1}{p_{i,O_2}}$, using that $i = 4FJ_{YSZ,O}$. As mentioned above, the measured mass transport polarisation resistance was higher compared with the calculated gas conversion resistance probably because not all of the inlet gas stream was converted due to incomplete mixing in the gas phase. The change in the oxygen partial pressure is therefore expected to be slightly higher, but still insignificant.

Below 10^{-3} bar, the measurement of the oxygen partial pressure using the closed-end tube type sensor is therefore mainly limited by the slow response of the gas phase mass transport processes.

5.6 Conclusion

The impedance of a porous Pt/YSZ electrode was measured at oxygen partial pressures between 10^{-6} and 0.2 bar and at temperatures between 500 and 950 °C. Between 10^{-6} and 10^{-4} bar, the polarisation resistance was found to be inversely proportional to the oxygen partial pressure and nearly temperature independent which indicates that the impedance was dominated by mass transport processes. Furthermore the polarisation resistance related to mass transport processes was found to be inversely proportional to the inlet gas flow rate, which is in accordance with the model of a stagnant gas layer where the change in oxygen partial pressure is determined by gas conversion.

The time constant related to the mass transport processes was found to be inversely proportional to and the capacitance independent of the oxygen partial pressure, which indicate that the response time of the sensor is inversely proportional to the oxygen partial pressure below 10^{-4} bar. The capacitance related to the mass transport processes was extraordinary high, around 0.01 F cm^{-2} between 10^{-4} and 10^{-6} bar.

The permeation of oxide ions through the sensor cell is not confined to the electrode area and increases the oxygen partial pressure of the process gas. However, the oxygen permeation is insignificant for an oxygen partial pressure of 10^{-6} bar between 600 and 800 °C using an inlet flow rate per unit area higher than 2 L $h^{-1}cm^{-2}$. For the particular kind of sensor geometry and electrode used here, the gas phase mass transport processes limits the measurement of the oxygen partial pressure.

5.7 Acknowledgements

This work was supported financially by The Programme Commission on Sustainable Energy and Environment, The Danish Council for Strategic Research, via the Strategic Electrochemistry Research Center (SERC) (www.serc.dk), contract no. 2104-06-0011.

CHAPTER 6

The composite Sr and V-doped $LaCrO_3$/YSZ electrode

The chapter should be submitted as A. Lund, T. Jacobsen, K. V. Hansen and M. Mogensen, "Composite Sr and V-doped $LaCrO_3$/YSZ oxygen sensor electrode"

6.1 Introduction

Perovskite-type metal oxides are promising candidates for high temperature potentiometric oxygen gas sensor electrodes and could thereby replace platinum which is more expensive and less abundant.[35,36,42] The oxygen reaction may take place at the surface/gas interface and these materials may be mixed ionic and electronic conductive. The reaction for the platinum electrode is con-

fined to the region near the triple phase boundary.[44,45,57] An electrode of a metal oxide may therefore have a higher active area compared with a platinum electrode and may therefore be more resistant towards poisoning by impurities. The metal oxide electrode should be chemically stable in contact with the electrolyte, the thermal expansion should match that of the yttria stabilised zirconia (YSZ) electrolyte and the volume should not expand significantly by uptake/release of oxygen.[23]

The potentiometric oxygen sensor is used because of its stability[3] in for example the food industry where oxygen is detrimental. The potentiometric oxygen sensor consists of two electrodes separated by an oxide ion conductive electrolyte, typically YSZ. The cell develops an electromotive force given by the difference in oxygen partial pressure between the electrodes. Only a very small current is running through the cell which should therefore be characterised at open circuit voltage. The response time, the time it takes to perform a measurement, and the accuracy depends on the electrode oxygen processes. The response time should not be more than a few seconds, similar to that of a platinum electrode. However, the electrode oxygen processes for metal oxide electrodes are not well described at low oxygen partial pressures around 10^{-6} bar, at which potentiometric oxygen sensors typically operate.

We have chosen to study the perovskite-type strontium and vanadium-substituted lanthanum chromite with the formula $La_{0.8}Sr_{0.2}Cr_{0.97}V_{0.03}O_{3-\delta}$ (LSCV), where δ is the deviation from stoichiometry. The strontium substitution induces oxide ion vacancies and electron holes which increases the oxide ion and electron hole conductivity, *p*-type conductivity, around 30 S cm^{-1} at 700 °C at an oxygen partial pressure of 1 bar.[50] The strontium substituted lanthanum chromite is not reduced significantly down to 10^{-16} bar at 1000 °C and has nearly the same thermal expansion coefficient as YSZ.[53] Chromium oxide is substituted with vanadium oxide to improve the sinterability which is also improved by mixing LSCV with YSZ to produce a composite electrode.[54,96]

The electrode oxygen processes can be characterised by electrochemical impedance spectroscopy (EIS) in a broad frequency range and thereby separate the oxygen processes by their characteristic frequency. The impedance spectra obtained from measurements on mixed ionic and electronic oxides can be modelled using a Gerischer-type impedance at high oxygen partial pressures.[57,62] Using this model, the oxygen reaction is related to surface kinetics and solid-state diffusion of oxide ions.[57] Measurements performed on platinum/YSZ cells, have shown that gas phase mass transport processes dominate the impedance spectrum at low oxygen partial pressures around 10^{-6}. The impedance of these

processes is inversely proportional to the oxygen partial pressure.[60] The electrochemical properties are dependent on the microstructure of the electrode, which can be characterised by electron microscopy.

The present paper seeks to evaluate the LSCV/YSZ composite electrode as a candidate for oxygen sensor electrodes. The oxygen processes at the electrode were characterised by performing electrochemical impedance spectroscopy (EIS) measurements between 600 and 900 °C at oxygen partial pressures between 4.2×10^{-6} and 0.2 bar. The microstructure of the electrode was characterised by electron microscopy.

6.2 Experimental

The $La_{0.8}Sr_{0.2}Cr_{0.97}V_{0.03}O_{3-\delta}$ (LSCV) powder was synthesized by pyrolysis of an aqueous solution of metal nitrates (>99% purity, Johnson Matthey) with glycine.[63] The powder was calcined at 800 °C for 2 h and the perovskite phase was verified by x-ray powder diffraction performed on a Theta-Theta STOE diffractometer. A paste of LSCV mixed with 8 mol% YSZ (99.85%, Tosoh Corp.) with a volume ratio between LSCV and YSZ of 1:1 was brush painted on a 3-electrode pellet, Figure 5.4, YSZ to produce a working electrode with an area of 0.39 cm^2. The 3-electrode pellet was painted two times and then sintered at 1200 °C in air for 2 h to produce a porous electrode, the working electrode of the 3-electrode pellet. The counter and reference electrodes were painted once on the 3-electrode pellet using a platinum paste and then sintered at 1000 °C for 2 h.

Figure 5.4 shows a cross section of the 3-electrode pellet of YSZ and the 3-electrode setup. The working electrode was placed in a controlled atmosphere of mixed dry N_2 and dry air. The oxygen partial pressure could be controlled between 0.2 bar and around 10^{-6} bar, with an accuracy of $\pm 10\%$, by mixing these gasses or supplying oxygen into flowing N_2 by an electrochemical pumping cell. The oxygen partial pressure at the counter and reference electrode was 0.2 bar. The inlet gas flow rate was between 8 and 15 L h^{-1}. The oxygen partial pressure at the working electrode was monitored by measuring the potential difference between the working and the reference electrode and the temperature, which was controlled with an accuracy of ± 1 ^{o}C. Furthermore, two potentiometric oxygen sensors were used to measure the oxygen partial pressure of the gas inlet and outlet.

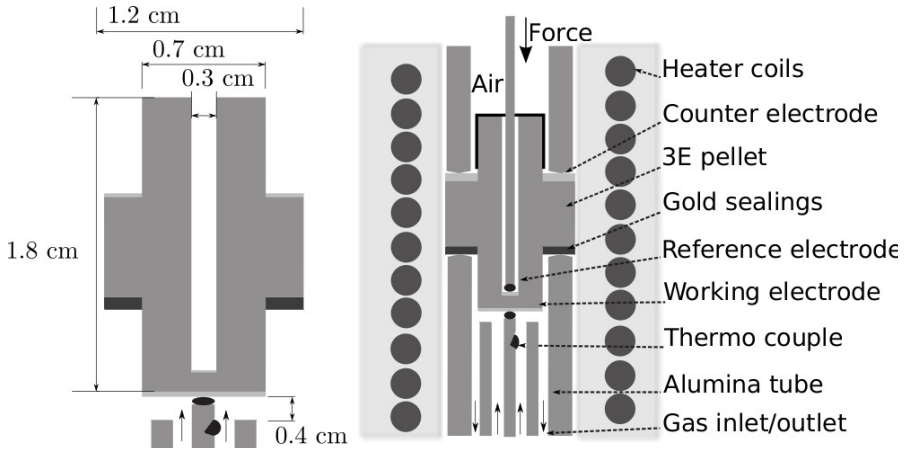

Figure 6.1: The cross section of the 3-electrode pellet and the test setup.

6.3 Results

6.3.1 Electrode microstructure

SEM images of the electrode were obtained using field emission SEM (Zeiss SUPRA-35) with a secondary electron (SE) detector. Figures 6.2 and 6.3 show SEM images of parts of the electrode, which has been cut by a diamond saw. Figure 6.2 shows that the electrode is around 15 µm thick and porous with sub-micrometer sized particles. The YSZ electrolyte is seen in the bottom part of the image. Figure 6.3 shows that LSCV and YSZ grains, between 200 and 400 nm in sizes, are agglomerated.

6.3.2 EIS measurements

EIS measurements were performed with a Solartron 1250 frequency response analyser and a Solartron 1287 potentiostat in a frequency range from 2×10^{-3} Hz to 10 kHz with 3 to 20 measurements per frequency decade at open circuit voltage with an AC root mean square amplitude of 10 mV. The measurements

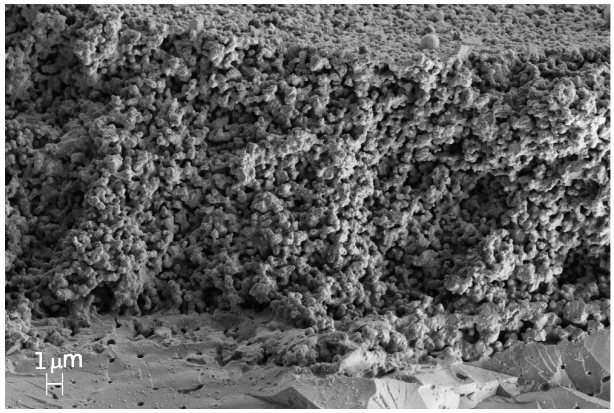

Figure 6.2: A scanning electron micrograph (SE2 detector) of the porous LSCV/YSZ working electrode.

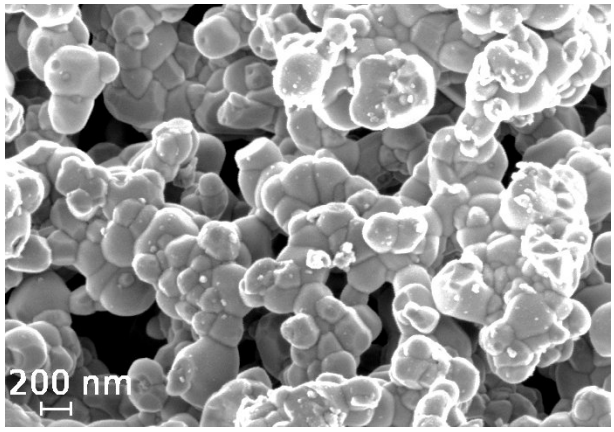

Figure 6.3: A scanning electron micrograph (SE Inlens detector) of the porous LSCV/YSZ working electrode.

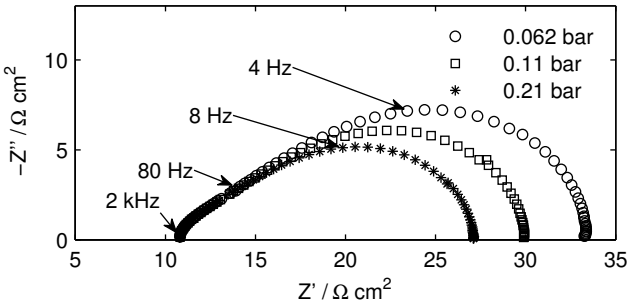

Figure 6.4: Nyquist plot for measurements performed at 700 ^{o}C and at an inlet flow rate of 8 L h^{-1} at various oxygen partial pressures.

were performed between 600 and 900 °C and between an oxygen partial pressure of 4.2×10^{-6} and 0.2 bar. The EIS data were fitted with equivalent circuit models using the Levenberg–Marquardt algorithm in Matlab.

Figure 6.4 shows that the impedance increases when the oxygen partial pressure is decreased from 0.21 to 0.062 bar at 700 °C. The impedance spectra consist of at least one depressed arc. In a range between 20 to 200 Hz, the impedance spectra present a straight line, which indicates that the processes at these frequencies are related to solid state diffusion of oxide ions.[57] This part of the impedance spectra does not depend on the oxygen partial pressure. The intersection between the impedance at around 2 kHz and the real-axis corresponds to the ohmic loss due transport of oxide through the YSZ electrolyte, around 10 Ω cm^2. The distance between the working and reference electrode is 0.2 cm, and a rough estimate of the conductivity of the YSZ is then $\sigma = 0.2/10$ S $cm^{-1} = 0.02$ S cm^{-1}, which is in accordance with the bulk oxide ion conductivity of YSZ at 700 °C.[80] The intersection between the impedance at low frequency and the x-axis of the Nyquist plot gives the DC resistance. The polarisation resistance related to the arc was found to be highly temperature dependent which also indicates that the arc represents oxygen reaction kinetics at the electrode.

Figure 6.5 shows that the impedance increases and the characteristic frequency decreases with decreasing oxygen partial pressure between 4.2×10^{-6} and $14 \times$

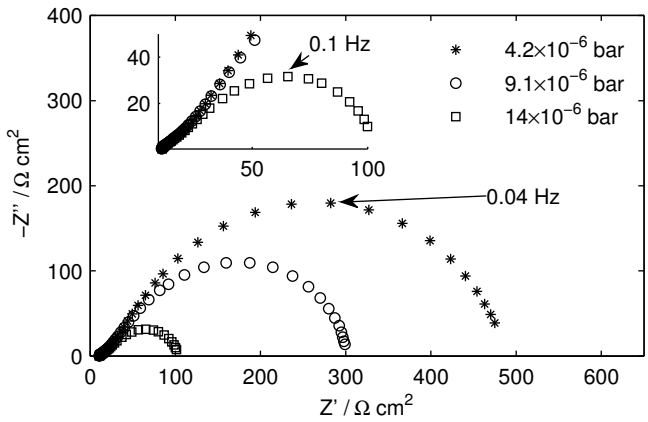

Figure 6.5: Nyquist plot for measurements performed at 700 ^{o}C and at an inlet gas flow rate of 8 L h^{-1} at various oxygen partial pressures.

10^{-6} bar at 700 °C and at an inlet flow rate of 8 L h^{-1}. The measured impedance is much more dependent on the oxygen partial pressure compared with the measurements performed between 0.062 and 0.2 bar. One depressed and nearly symmetrical arc dominates the impedance at 4.2×10^{-6} bar with a characteristic frequency of around 0.04 Hz.

Figure 6.6 shows that the polarisation resistance, R_{p}, is proportional to $p_{\mathrm{O_2}}^{-0.25}$ between oxygen partial pressures of 0.2 and around 10^{-5} bar. Below 10^{-5} bar, the slope increases which indicates that gas mass transport processes are dominating.

The impedance was measured at various temperatures at an oxygen partial pressure of 10^{-5} bar and at an inlet gas flow rate of 8 L h^{-1}. Figure 6.7 shows an Arrhenius plot of the polarisation resistance. The slope increases with decreasing temperature probably because the oxygen reaction dominates the polarisation resistance at low temperatures and the gas phase mass transport processes dominate the polarisation resistance at high temperatures. The resistance related to gas phase mass transport processes is nearly temperature independent. The slope of the graph at 650 °C corresponds to an activation energy of 1 eV.

Gas phase mass transport by convection is inversely proportional to the inlet gas flow rate.[60,89] Figure 6.8 indicates that the polarisation resistance is in-

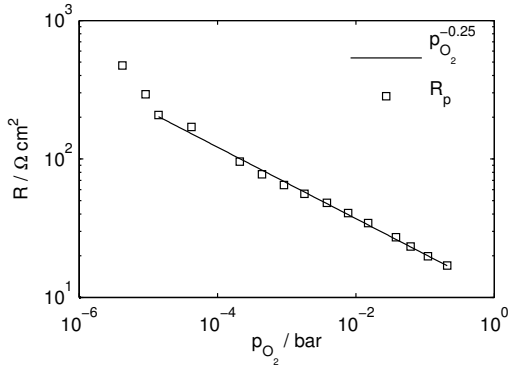

Figure 6.6: The polarisation resistance, R_p, as a function of the oxygen partial pressure for measurements performed at 700 °C and at an inlet gas flow rate of 8 L h^{-1}.

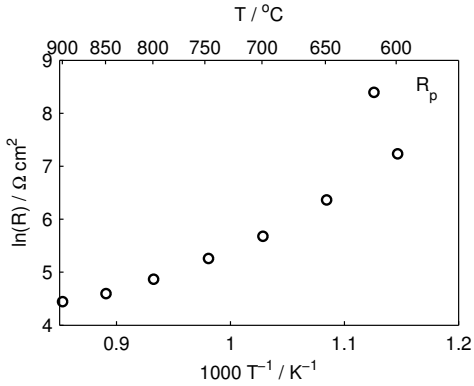

Figure 6.7: Arrhenius plot of the polarisation resistance for measurements performed at an oxygen partial pressure of 10^{-5} bar and at an inlet gas flow rate of 8 L h^{-1}.

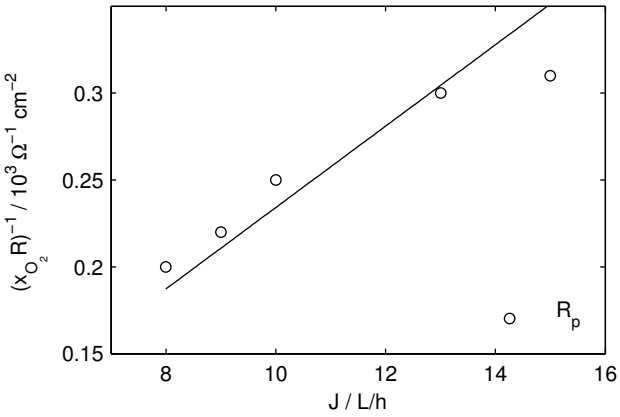

Figure 6.8: The inverse of the normalised polarisation resistance, $(R_p x_{O_2})^{-1}$, as a function of the inlet gas flow rate for measurements performed at an oxygen partial pressures of 3×10^{-5} bar at 800 °C. The solid line is a linear fit going through the origo.

versely proportional to the inlet gas flow rate for measurements performed at an oxygen partial pressure of around 3×10^{-5} bar, at 800 °C. The polarisation resistance was multiplied with the oxygen mole fraction $x_{O_2} = p_{O_2}/P$, where P is the atmospheric pressure, to account for variations in the oxygen partial pressure. The polarisation resistance is assumed to be dominated by gas phase mass transport processes, for which the impedance is inversely proportional to the oxygen partial pressure. For example the gas conversion resistance is give by[89]

$$R_C = \frac{PRT}{16F^2} \frac{1}{J_i} \frac{1}{p_{i,O_2}} \tag{6.1}$$

where R is the gas constant, T is the temperature, F is Faradays constant and J_i is the inlet gas flow rate per unit area and p_{i,O_2} is the inlet oxygen partial pressure. The results indicate that mass transport processes therefore dominate the impedance at low oxygen partial pressures.

6.4 Discussion

6.4.1 $p_{O_2} > 10^{-4}$ bar

The impedance spectra were analysed with equivalent circuit modelling to separate and identify the processes contributing. The impedance of a porous mixed ionic and electronic conducting electrode is equivalent to that of a Gerischer element assuming that the AC penetration depth is short compared with the thickness of the electrode[57]

$$Z_{\mathrm{MIEC}} = R_{\mathrm{e}} \left(\frac{1}{1 + (\tau_{\mathrm{e}} i\omega)^{n_{\mathrm{e}}}} \right)^{1/2} \tag{6.2}$$

where R_{e} represents the polarisation resistance which include both surface kinetics and solid state transport of oxide ions, $\tau_{\mathrm{e}} = 1/k_{\mathrm{e}}$ is the time constant related to the surface reaction kinetics, which is equal to the inverse of the reaction rate constant, and n_{e} is an exponent which is included to take into account a depression of the arcs in the Nyquist plot.[61] The impedance spectra obtained at these oxygen partial pressures were fitted with an equivalent circuit model, $(R_{\mathrm{s}})(L)(G)$, which consists of a Gerischer element, G, connected in series with a resistor R_{s} and an inductance, L. The series resistance represents the ohmic loss due to transport of oxide ions in the YSZ electrolyte. The inductance is included to take into account the high frequency inductance and instrumental artefacts. Figure 6.9 shows the Nyquist plot for a measurement performed at 0.2 bar and the corresponding model fit. The impedance shown has been normalised with respect polarisation resistance and the series resistance has been subtracted.

The frequency dependent part is raised to the power of n_{e}, to take into account the depression of the arcs.[77] The model then has 5 free parameters where only 3 are related to the oxygen reaction. At 0.2 bar, an inlet flow rate of 8 L h^{-1} between 600 and 900 °C, n_{e} was found to be 0.88 ± 0.03. The apparent activation energy of R_{e} was found to be 1.60 ± 0.03 eV and that of τ_{e} was found to be 1.80 ± 0.05 eV. The polarisation resistance was found to be proportional to $p_{O_2}^{-0.25}$ at 700 °C. The time constant was found to be proportional to $p_{O_2}^{-0.5}$ and the reaction rate constant was proportional to $p_{O_2}^{0.5}$. A similar dependency of the oxygen partial pressure and the activation energy has previously been observed for other perovskite-type metal oxides.[30,57,97] The summit frequency is among others highly dependent on the sintering temperature and the thickness of the electrode.[97] For composite perovskite-type electrodes which have been

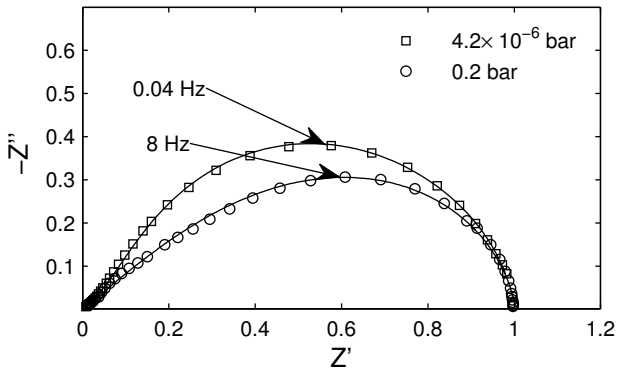

Figure 6.9: Nyquist plot of the impedance, normalised with respect to the polarisation resistance and corrected for the series resistance, for measurements performed at 700 °C, an oxygen partial pressure of 0.2 and 4.2×10^{-6} bar and at an inlet gas flow rate of 8 L h^{-1}, with fits.

sintered at similar temperatures with similar electrode thicknesses, the summit frequencies are nearly the same.[56,97]

6.4.2 $p_{O_2} < 10^{-4}$ bar

The model applied at oxygen partial pressures below 10^{-4} bar has an extra RC-circuit, $(R_{mt}C_{mt})$ connected in series, which represents mass transport processes. R_{mt} is the polarisation resistance and C_{mt} the capacitance related to the mass transport processes.[60,89] The capacitance, C_{mt}, was replaced by a constant phase element, Q_{mt} to take into account a depression of the arcs observed.[77] The depression of the arcs was assumed to be similar, $n_{mt} = n_e$, and constrained so that $0.9 < n_e, n_{mt} < 1$ while fitting to decrease the number of free parameters. Furthermore, the constraint $\tau_{mt} > \tau_e$ was applied because the mass transport processes are always slower than the oxygen reaction at transient conditions because it is the oxygen reaction which initiates the transport processes. The model, $(R_s)(L)(G)(R_{mt}Q_{mt})$, therefore has 6 free parameters. The fits are shown with solid line in Figure 6.9. The capacitance of the mass transport processes is given by $C_{mt} = (R_{mt}^{1-n_{mt}}Q_{mt})^{1/n_{mt}}$,[77] where Q_{mt} is a constant phase element and the gas phase mass transport time constant is given by $\tau_{mt} = R_{mt}C_{mt}$.

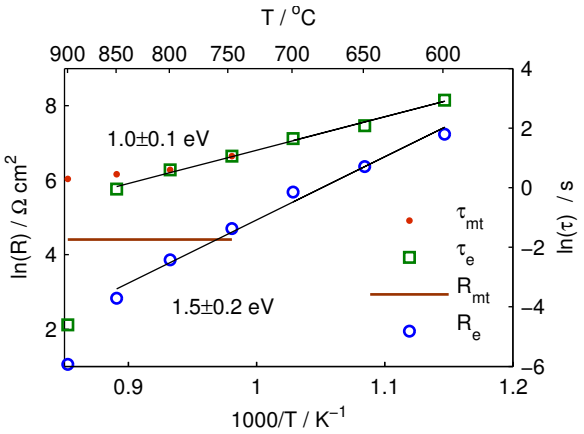

Figure 6.10: Arrhenius plot of the time constant and the polarisation resistance at an oxygen partial pressure of 10^{-5} bar and $J_i = 8$ L h^{-1}.

Figure 6.7 shows the polarisation resistance as function of the inverse temperature at an oxygen partial pressure of 10^{-5} bar and an inlet gas flow rate of 8 L h^{-1}. At 900 °C, the polarisation resistances R_{mt} and R_e were found to be 82 and 2.2 Ω cm^2, respectively, and the polarisation resistance increased only slightly with temperature. The polarisation resistance related to gas conversion can be calculated to be $R_C = \frac{PRT}{16F^2}\frac{1}{J_i}\frac{1}{p_{i,O_2}} = 27$ Ω cm^2 where $J_i = 8/0.39$ L h^{-1} cm^{-2} and $p_{i,O_2} = 10^{-5}$ bar.[60] The measured gas conversion resistance is higher because only a part of the inlet gas is converted, probably due to incomplete mixing in the gas space above the working electrode. The polarisation resistance related to the mass transport processes is assumed to be independent of the temperature and the value of R_{mt}, obtained at 900 °C, was therefore used when fitting the impedance measured at lower temperatures to decrease the number of free parameters.

Below 700 °C, the oxygen reaction kinetics dominated the impedance and the gas phase mass transport processes were not observed. The Arrhenius plot in Figure 6.10 shows that the apparent activation energy of R_e is 1.5 ± 0.2 eV and that of τ_e, is 1.0 ± 0.1 eV. It is also seen that between 750 and 800 °C, it is not possible to separate the time constants of the mass transport processes and the oxygen reaction because the arcs related to these processes overlap in the impedance spectrum. The activation energy of τ_e is decreased compared with the measurements performed at 0.2 bar while that of R_e did not change significantly. At 700 °C, it was not possible to separate the arc related to mass transport processes and that related to the oxygen reaction. However,

the Nyquist plot in Figure 6.5 indicates that mass transport processes become dominating at an oxygen partial pressure around 10^{-5} bar. R_{mt} was therefore determined from two measurements performed below an oxygen partial pressures of 10^{-5} bar at 700 °C. The resistance related to the oxygen reaction, R_e, was extrapolated from the measurements performed at higher oxygen partial pressure. Figure 6.11 indicates that R_{mt} is highly dependent on the oxygen partial pressure, as expected and at 4.2×10^{-6} bar R_{mt} and R_e were found to be nearly equal. The Figure also shows that it as not possible to separate the time constants related to the oxygen reaction and the gas phase mass transport processes. The graph indicates that the time constants of the mass transport processes increases with decreasing oxygen partial pressure.

Theoretically, the gas conversion resistance gives rise to a symmetrical semicircle and the resistance is inversely proportional to the oxygen partial pressure, but the time constant should be independent.[60] The gas conversion time constant is related to the volume of the gas layer as $\tau_C = \frac{J_i RT}{P} V_C$,[60] where V_C is the volume of the gas layer, J_i is in the inlet gas flow rate, R is the gas constant, T is the temperature and P is the atmospheric pressure. The volume of the gas layer may then be calculated, if the measured mass transport time constant is equal to the gas conversion time constant, to be 29 cm^3, which does not fit with the dimensions of the 3-electrode setup. The LSCV stores oxygen by changing stoichiometry and the differential capacitance associated with the change in stoichiometry is given by

$$C = -V_{LSCV} 2F \frac{dc_V}{dE} \tag{6.3}$$

where c_V is the concentration of oxide ion vacancies and V_{LSCV} is the volume of the inactive LSCV, which is assumed to be approximately the volume of LSCV, $V_{LSCV} = V_{electrode}\phi_{LSCV} = 15{\times}10^{-4}$ cm $\times\, 0.39$ $cm^2 \times 1/3 = 1.9 \times 10^{-4}$ cm^3, where $\phi_{LSCV} = 1/3$ is the volume fraction of LSCV. Assuming equilibrium is obtained the potential differentiated with respect to the oxygen partial pressure is given by $dE = \frac{RT}{4F}\frac{1}{p_{O_2}} dp_{O_2}$. The differential capacitance may then be calculated using that

$$C = -V_{LSCV} 2F \frac{dc_V}{dE} = -V_{LSCV} \frac{8F^2}{RT} p_{O_2} \frac{d(\beta p_{O_2}^{-0.5})}{dp_{O_2}} = V_{LSCV} \frac{4F^2}{RT} c_V \tag{6.4}$$

where β is some constant. The vacancy concentration is nearly proportional to $p_{O_2}^{-0.5}$ at these oxygen partial pressures.[59] At 700 °C and an oxygen partial pressure of 4.2×10^{-6} bar, the concentration of vacancies was calculated according to Van Hassel *et al.*[59] at 1000 °C to be 3.8×10^{-7} mole cm^{-3} and the calculated capacitance was then 3×10^{-4} F cm^{-2} which is a lower compared with the measured capacitance, $C_{mt} = 0.02$ F cm^{-2}.

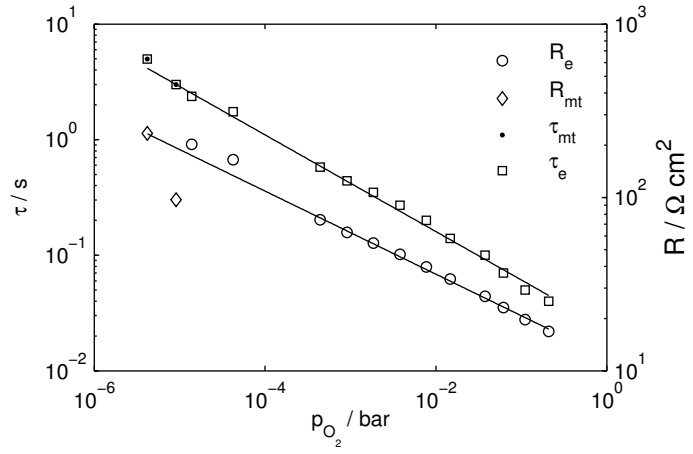

Figure 6.11: The time constant and capacitance as functions of the oxygen partial pressure for measurements performed at 700 °C at an inlet gas flow rate of 8 L h^{-1}.

6.5 Conclusion

The electrochemical properties of a porous composite LSCV/YSZ electrode was characterised by EIS at various oxygen partial pressures, temperatures and inlet gas flow rates. The electrode was found to have a porous coherent structure with LSCV and YSZ grain sizes between 200 and 400 nm. At oxygen partial pressures around 0.2 bar, the oxygen reaction is dominated by solid state diffusion of oxide ions and surface kinetics and the reaction rate constant related to the surface kinetics is proportional to $p_{O_2}^{0.5}$ and has an activation energy of 1.8 eV.

At low oxygen partial pressures around 10^{-5} bar above 800 °C, gas phase mass transport processes dominate the impedance spectra and the impedance is inversely proportional to the inlet gas flow rate. The activation energy of the time constant related to the surface reaction kinetics was found to be 1 eV. The polarisation resistance and the time constant of the dominating arc increased with decreasing oxygen partial pressure. LSCV may take up/release oxygen by changing the oxide ion stoichiometry, which gives a large capacitance. The relatively low time constant, around 5 s at 700 °C at an oxygen partial pressure of around 5×10^{-6} bar, makes the LSCV/YSZ electrode suitable for use as an industrial oxygen sensor electrode.

6.6 Acknowledgements

This work was supported financially by The Programme Commission on Sustainable Energy and Environment, The Danish Council for Strategic Research, via the Strategic Electrochemistry Research Center (SERC) (www.serc.dk), contract no. 2104-06-0011.

CHAPTER 7

Conclusion

Electrode materials have been evaluated as candidates for oxygen sensor electrodes and the thesis presents the electrochemical properties of a LSCV/YSZ composite electrode and three different platinum-based electrodes; the single phase platinum electrode, the cermet CGO impregnated platinum electrodes and the cermet Pt/YSZ electrode. The development of the electrode materials was carried out in a collaboration with PBI-Dansensor and the electrodes were therefore similar to the type of electrode which is currently used by the company, the single phase platinum electrode. The electrochemical properties were characterised by electrochemical impedance spectroscopy at temperatures from around 500 up to 900 °C at oxygen partial pressures between 10^{-6} and 0.2 bar. The microstructure and the morphology was characterised with electron microscopy. At an oxygen partial pressure of 0.2 bar, the response time of the all the electrodes investigated was determined by oxygen reaction kinetics. At oxygen partial pressures around 10^{-6} bar at 700 °C, the mass transport processes dominated the response time which increased with decreasing oxygen partial pressure and decreasing inlet gas flow rate.

The images of the CGO impregnated platinum electrodes, obtained by electron microscopy, showed that CGO was found as porous agglomerates in the

pores of the electrode and for some electrodes with a high loading as a layer on the platinum surface. The impedance spectra obtained from measurements on the impregnated electrodes showed that a part of the oxygen reaction involved transport of oxide ions in the CGO phase. Therefore, the addition of CGO increased the effective TPB length and the impregnated electrode may therefore be more robust towards poisoning by impurities compared with the single phase platinum electrode. The polarisation resistance was decreased by increasing the annealing temperature of the CGO impregnated electrodes which was interpreted as due to an increased oxide ion conductivity of the percolating CGO phase.

At 0.2 bar, the addition of CGO decreased the activation energy of the oxygen reaction from 2 eV for the single phase platinum electrode to between 1.2 and 1.5 eV for the impregnated electrodes. The activation energy of the oxygen reaction was found to be 1.9 and 1.8 eV for the Pt/YSZ and the LSCV/YSZ composite electrode, respectively. The characteristic frequency of the arc related to the oxygen reaction was found to be 500 Hz for the single phase electrode, between 500 and 2000 Hz for the impregnated electrodes, 60 Hz for the Pt/YSZ electrode and 8 Hz for the LSCV/YSZ electrode. At 700 °C, the polarisation resistance, of one electrode, could be decreased from 2 Ω cm^2 for the single phase platinum electrode to 0.3 Ω cm^2 by impregnation with CGO and the polarisation resistance was found to be 2 Ω cm^2 and 17 Ω cm^2 for the Pt/YSZ and the LSCV/YSZ composite electrode, respectively. This shows that the LSCV/YSZ electrode is not a good catalyst for the oxygen reaction and has a slower response time compared to the platinum-based electrodes. The oxygen reaction at the Pt/YSZ , the LSCV/YSZ composite and some of the CGO impregnated electrodes involved solid state diffusion of oxide ions and surface reaction kinetics. Thus it indicates that the these electrodes have a large active area and may therefore be more robust compared with the single phase platinum electrode.

At an oxygen partial pressure of 5×10^{-5} bar, at 700 °C, the time constant of the dominating was between 0.4 and 0.8 s for both the impregnated and the single phase platinum electrode and around 0.8 s for the Pt/YSZ electrode. At 700 °C and an oxygen partial pressure of 5×10^{-6} bar, the time constant of the dominating arc was found to be 5 s and 0.5 s for the LSCV/YSZ electrode and the Pt/YSZ electrode, respectively. The response time of the LSCV/YSZ electrode, $2\tau = 10$ s at 700 °C and 5×10^{-6} bar, is therefore an order of magnitude longer compared to that of the platinum-based electrodes probably because LSCV can take up/release oxygen by changing the oxide ion stoichiometry.

Even though the response time of the LSCV/YSZ electrode is longer compared with that of a single phase electrode, the electrode may be more robust against poisoning by impurities because of its large active area, compared with the single phase platinum electrode. The effective TPB of the platinum electrode could be increased, either by impregnation with CGO or by mixing platinum with YSZ, without increasing the response time at low oxygen partial pressures, where it becomes critical.

Bibliography

1. A. Mills, *Chemical Society reviews*, **34**, 1003 (2005).

2. N. Docquier and S. Candel, *Progress in Energy and Combustion Science*, **28**, 107 (2002).

3. P. Shuk, E. Bailey, and U. Guth, *Sensors (Peterborough, NH)*, **90**, 174 (2008).

4. R. C. Evans, P. Douglas, J. A. G. Williams, and D. L. Rochester, *Journal of Fluorescence*, **16**, 201 (2006).

5. J. Weissbart and R. Ruka, *Review of Scientific Instruments*, **32**, 593 (1961).

6. U. Guth, W. Vonau, and J. Zosel, *Measurement Science and Technology*, **20**, 042002 (2009).

7. W. Göpel and K.-D. Schierbaum, "Specific Molecular Interactions and Detection Principles," in *Sensors: A Comprehensive Survey*, edited by Göpel, W. and Hesse, J. and Zemel, N. J. (Wiley-VCH Verlag GmbH, 2008) pp. 119–157.

8. R. Moos, *International Journal of Applied Ceramic Technology*, **2**, 401 (2005).

9. H. Wiemhöfer and K. Cammann, "Specific features of electrochemical sensors," in *Sensors: A Comprehensive Survey*, edited by Göpel, W. and Hesse, J. and Zemel, N. J. (Wiley Online Library, 1991) pp. 159–189.

10. U. Röder-Roith, F. Rettig, T. Röder, J. Janek, R. Moos, and K. Sahner, *Sensors and Actuators B: Chemical*, **136**, 530 (2009).

11. J. Spirig, R. Ramamoorthy, S. Akbar, J. Routbort, D. Singh, and P. Dutta, *Sensors and Actuators B: Chemical*, **124**, 192 (2007).

12. J. R. Stetter and J. Li, *Chemical reviews*, **108**, 352 (2008).

13. C. Alcock, *Solid State Ionics*, **56**, 3 (1992).

14. A. Anthony, J. Baumard, and J. Corish, *Solid State Ionics*, **56** (1984).

15. S. Badwal, M. Bannister, F. Ciacchi, and G. Hooshmand, *Journal of Applied Electrochemistry*, **18**, 608 (1988).

16. D. Baker, *AIChE journal*, **40**, 1498 (1994).

17. J. Fouletier, E. Mantel, and M. Kleitz, *Solid State Ionics*, **6**, 1 (1982).

18. J. Fouletier, *Sensors and Actuators*, **3**, 295 (1983).

19. W. C. Maskell and B. C. H. Steele, *Journal of Applied Electrochemistry*, **16**, 475 (1986).

20. T. Etsell and S. Flengas, *Metallurgical and Materials Transactions B*, **3**, 27 (1972).

21. S. Badwal, *Solid State Ionics*, **52**, 23 (1992).

22. U. Messerschmidt, D. Baither, B. Baufeld, and M. Bartsch, *Materials Science and Engineering A*, **233**, 61 (1997).

23. P. Gellings and H. Bouwmeester, *The CRC handbook of solid state electrochemistry* (CRC, 1997) ISBN 0849389569.

24. M. Kleitz, T. Iharada, F. Abraham, G. Mairesse, and J. Fouletier, *Sensors and Actuators B: Chemical*, **13**, 27 (1993).

25. J. Ehrhardt, L. Colin, and D. Jamois, *Sensors and Actuators B: Chemical*, **40**, 117 (1997).

26. C. Park and S. Akbar, *Journal of Materials Science*, **38**, 4611 (2003).

27. T. Arakawa, A. Saito, and J. Shiokawa, *Bulletin of the Chemical Society of Japan*, **55**, 2273 (1982).

28. T. Inoue, N. Seki, K. Eguchi, and H. Arai, *Journal of the Electrochemical Society*, **137**, 2523 (1990).

29. T. H. Etsell, "Performance of Solid Oxide Fuel Cell Electrodes," in *Proceedings of the Workshop on High Temperature Solid Oxide Fuel Cells*, edited by H. S. Isaacs, S. Srinivasan, and I. L. Harr (Brookhaven National Laboratory, Long Island, NY, 1978) pp. 66–82.

30. S. B. Adler, *Chemical reviews*, **104**, 4791 (2004).

31. D. Haaland, *Journal of the Electrochemical Society*, **127**, 796 (1980).

32. C. Cullis and B. Willatt, *Journal of Catalysis*, **86**, 187 (1984).

33. M. a. Peña and J. L. Fierro, *Chemical reviews*, **101**, 1981 (2001).

34. U. Lampe, M. Fleischer, and N. Reitmeier, *Sensors*, **2**, 1 (1996).

35. C. B. Alcock, *Solid State Ionics*, **51**, 281 (1992).

36. S. Badwal, F. Ciacchi, and J. Haylock, *Journal of Applied Electrochemistry*, **18**, 232 (1988).

37. J. W. Fergus, *Sensors and Actuators B: Chemical*, **123**, 1169 (2007).

38. R. Meyer and R. Waser, *Sensors and Actuators B: Chemical*, **101**, 335 (2004).

39. R. Ramamoorthy, S. Akbar, and P. Dutta, *Sensors and Actuators B: Chemical*, **113**, 162 (2006).

40. H. Song, J. Moon, and H. Hwang, *Journal of the European Ceramic Society*, **26**, 981 (2006).

41. H. Wiemhöfer, *Solid State Ionics*, **175**, 93 (2004).

42. G. Barbi, A. Casiraghi, and C. Mari, *Review of Scientific Instruments*, **54**, 486 (1983).

43. E. Mutoro, B. Luerß en, S. Günther, and J. Janek, *Solid State Ionics*, **180**, 1019 (2009).

44. A. Mitterdorfer and L. Gauckler, *Solid State Ionics*, **117**, 187 (1999).

45. A. Mitterdorfer and L. Gauckler, *Solid State Ionics*, **117**, 203 (1999).

46. "Kitco www.kitco.com," (2011).

47. "Metal-pages www.metal-pages.com," (2011).

48. J. Lee, *Journal of Materials Science*, **38**, 4247 (2003).

49. D. Meadowcroft, *Journal of Physics D: Applied Physics*, **2**, 1225 (1969).

50. D. Karim and A. Aldred, *Physical Review B*, **20**, 2255 (1979).

51. J. R. m. Hansen, *Strontium and Vanadium Doped Lanthanum Chromites for Interconnector Material in Solid Oxide Fuel Cells*, Ph.D. thesis, Technical University of Denmark (2000).

52. T. Nakamura, G. Petzow, and L. Gauckler, *Materials Research Bulletin*, **14**, 649 (1979).

53. J. Fergus, *Solid State Ionics*, **171**, 1 (2004).

54. P. Larsen, P. Hendriksen, and M. Mogensen, *Journal of Thermal Analysis and Calorimetry*, **49**, 1263 (1997).

55. A. Brailsford and E. Logothetis, *Sensors and Actuators B: Chemical*, **52**, 195 (1998).

56. E. Murray, T. Tsai, and S. Barnett, *Solid State Ionics*, **110**, 235 (1998).

57. S. Adler, J. Lane, and B. Steele, *Journal of the Electrochemical Society*, **143**, 3554 (1996).

58. J. Mizusaki, *Solid State Ionics*, **52**, 79 (1992).

59. B. Van Hassel, T. Kawada, N. Sakai, H. Yokokawa, M. Dokiya, and H. Bouwmeester, *Solid State Ionics*, **66**, 295 (1993).

60. T. Jacobsen, P. Hendriksen, and S. Koch, *Electrochimica Acta*, **53**, 7500 (2008).

61. E. Barsoukov and J. R. Macdonald, *Impedance Spectroscopy Theory, Experiment, and Applications*, 2nd ed. (John Wiley & Sons, New Jersey, 2005).

62. A. Lasia, "Modeling of Impedance of Porous Electrodes," in *Modeling and Numerical Simulations* (Springer, 2009) pp. 67–137.

63. L. Chick, L. Pederson, G. Maupin, J. Bates, L. Thomas, and G. Exarhos, *Materials Letters*, **10**, 6 (1990).

64. J. L. Rupp, A. Infortuna, and L. J. Gauckler, *Acta Materialia*, **54**, 1721 (2006).

65. J. Winkler, P. Hendriksen, N. Bonanos, and M. Mogensen, *Journal of the Electrochemical Society*, **145**, 1184 (1998).

66. M. Mogensen, N. Sammes, and G. Tompsett, *Solid State Ionics*, **129**, 63 (2000).

67. B. Steele, *Solid State Ionics*, **129**, 95 (2000).

68. T. Suzuki, I. Kosacki, and H. Anderson, *Journal of the American Ceramic Society*, **85**, 1492 (2002).

69. A. Trovarelli, *Catalysis by ceria and related materials* (World Scientific Publishing Company, 2002) ISBN 1860942997.

70. K. Patil, *Combustion* (World Scientific Publishing Company, 2008).

71. P. Blennow, K. Hansen, L. Wallenberg, and M. Mogensen, *Journal of the European Ceramic Society*, **27**, 3609 (2007).

72. S. P. Jiang, X. J. Chen, S. H. Chan, and J. T. Kwok, *Journal of the Electrochemical Society*, **153**, A850 (2006).

73. X. Chen, Q. Liu, S. Chan, N. Brandon, and K. Khor, *Electrochemistry Communications*, **9**, 767 (2007).

74. A. Barbucci, R. Bozzo, and G. Cerisola, *Electrochimica Acta*, **47**, 2183 (2002).

75. O. J. Velle and T. Norby, *Solid State Ionics*, **52**, 93 (1992).

76. G. Brauer and H. Gradinger, *Zeitschrift fuer anorganische und allgemeine Chemie*, **276**, 209 (1954).

77. M. E. Orazem and B. Tribollet, *Electrochemical Impedance Spectroscopy* (John Wiley & Sons, New Jersey, 2008) p. 236.

78. A. K. Opitz and J. Fleig, *Solid State Ionics*, **181**, 684 (2010).

79. C. Hitz and a. Lasia, *Journal of Electroanalytical Chemistry*, **500**, 213 (2001).

80. S. Badwal, *Journal of Materials Science*, **19**, 1767 (1984).

81. C. Levy, C. Guizard, and A. Julbe, *Journal of the American Ceramic Society*, **90**, 942 (2007).

82. S. Primdahl and M. Mogensen, *Journal of the Electrochemical Society*, **146**, 2827 (1999).

83. A. Bernasik, *Journal of Physics and Chemistry of Solids*, **63**, 233 (2002).

84. A. Hughes and S. Badwal, *Solid State Ionics*, **46**, 265 (1991).

85. W. Göpel, T. A. Jones, J. N. Zemel, and T. Seiyama, "Historical remarks," in *Sensors: A comprehensive survey*, edited by W. Göpel, J. Hesse, and N. J. Zemel (Wiley Online Library, 1991) pp. 29–59.

86. T. M. Gur, *Journal of the Electrochemical Society*, **127**, 2620 (1980).

87. M. Mori, H. Nishimura, Y. Itagaki, Y. Sadaoka, and E. Traversa, *Sensors and Actuators B: Chemical*, **143**, 56 (2009).

88. J. Park and R. Blumenthal, *Journal of the Electrochemical Society*, **136**, 2867 (1989).

89. S. Primdahl and M. Mogensen, *Journal of the Electrochemical Society*, **145**, 2431 (1998).

90. H. Okamoto, G. Kawamura, and T. Kudo, *Electrochimica Acta*, **28**, 379 (1983).

91. D. Y. Wang, *Journal of the Electrochemical Society*, **126**, 1155 (1979).

92. E. Fuller and P. Schettler, *Industrial & Chemical Engineering*, **58**, 18 (1966).

93. J. Kilner, in *Proc. of the 2nd Int. Symp. On Ionic and Mixed Conducting Ceramics* (1995) pp. 94–12.

94. P. Manning, J. Sirman, R. De Souza, and J. Kilner, *Solid State Ionics*, **100**, 1 (1997).

95. K. Sasaki, *Solid State Ionics*, **161**, 145 (2003).

96. S. Primdahl, J. Hansen, and L. Grahl-Madsen, *Journal of the Electrochemical Society*, **148**, 74 (2001).

97. M. Joergensen and M. Mogensen, *Journal of the Electrochemical Society*, **148**, A433 (2001).